FINAL REPORT

ON

NONLINEAR DYNAMICAL CONTROL OF LASERS

CONTRACT #N00014-93-C-0053

ITEM NO. 0001AD

DTIC
S ELECTE
DEC 0 2 1993
E
D

PREPARED FOR

OFFICE OF NAVAL RESEARCH
BALLSTON TOWER ONE
800 N. QUINCY STREET
ARLINGTON, VA 22217-5660

PREPARED BY

SCHWARTZ ELECTRO-OPTICS, INC.
3404 N. ORANGE BLOSSOM TRAIL,
ORLANDO, FL 32804

30 OCTOBER 1993

93 11 1 084

DISCLAIMER NOTICE

THIS DOCUMENT IS BEST QUALITY AVAILABLE. THE COPY FURNISHED TO DTIC CONTAINED A SIGNIFICANT NUMBER OF COLOR PAGES WHICH DO NOT REPRODUCE LEGIBLY ON BLACK AND WHITE MICROFICHE.

FINAL REPORT

ON

NONLINEAR DYNAMICAL CONTROL OF LASERS

CONTRACT #N00014-93-C-0053

ITEM NO. 0001AD

Accesion For		
NTIS CRA&I		☑
DTIC TAB		☑
Unannounced		☐
Justification		
By		
Distribution /		
Availability Codes		
Dist	Avail and / or Special	
A-1		

PREPARED FOR

OFFICE OF NAVAL RESEARCH
BALLSTON TOWER ONE
800 N. QUINCY STREET
ARLINGTON, VA 22217-5660

PREPARED BY

DTIC QUALITY INSPECTED 1

SCHWARTZ ELECTRO-OPTICS, INC.
3404 N. ORANGE BLOSSOM TRAIL,
ORLANDO, FL 32804

Statement A per telecon
Henschel Pilloff ONR/Code 1112
Arlington, VA 22217-5000

NWW 12 2/93

30 OCTOBER 1993

LIST OF FIGURES (CONT.)

LIST OF TABLES

TABLE OF CONTENTS

LIST OF FIGURES

1.0 INTRODUCTION

Schwartz Electro-Optics, Inc. (SEO) was awarded this Small Business Innovation Research (SBIR) Phase I program entitled, Nonlinear Dynamical Control of Laser under Contract No. N00014-93-C-0053 from the Office of Naval Research (ONR), Arlington, VA. SEO successfully demonstrated stable blue-green output via second harmonic generation (SHG) from a solid state laser using a $KNbO_3$ crystal in an external resonant cavity. The experiments were conducted at SEO, Orlando, Florida while the computer modelling was subcontracted to Dr. Donna Bandy's group at Oklahoma State University (OSU). The physics of lasers and SHG devices and their combination, naturally involves random chaotic fluctuations that can be attributed to the system nonlinearities. Contolling this behavior is demonstrated and a fundamental understanding of the role of the nonlinearities is exploited.

This final report provides a summary of work performed during 24 April 1993 through 23 October 1992. This program was completed on schedule and within the budget achieving all program objectives. In this introduction section of the report, background of the chaos-instabilities observed in the SHG process are discussed. Section 2.0, describes the experimental set-up. The results obtained are outlined in Section 3.0. The summary and conclusions are provided in section 4.0 of the report. Section 5.0 provides a brief outline of Phase II program plans.

1.1 CHAOS

The subject of Chaos has been investigated since the turn of the century, with much of the early work done by Paincare'. It wasn't until the recent advances in Chaos that the importance and scope of the field was realized. There is a wide variety of systems (in nature and man-made) that exhibit chaotic behavior, for example planetary orbits, convection in fluids, heating of plasmas, weather systems, chemical reactions, etc. It was earlier believed that these random variations were too complicated to describe mathematically and statistical descriptions where the only means of understanding these dynamic systems. Now it is known that these Chaotic system are not just random fluctuations but are totally deterministic. More importantly they can be controlled by studying the nature of the Chaos and applying small perturbations to the systems parameters.

1.2 CONTROL OF CHAOS

An excellent simple example of how Chaos can be controlled was carried out by Singer et al [ref 1]. They used a thermal convection loop with half the loop heated and the other half cooled. They studied the temperature fluctuations and convection flow in the liquid inside the loop by monitoring the temperature difference of the liquid on the cooled and heated areas. They found that there was rate of heat threshold at which the system would go from stable to Chaotic. By a simple feedback loop, from the
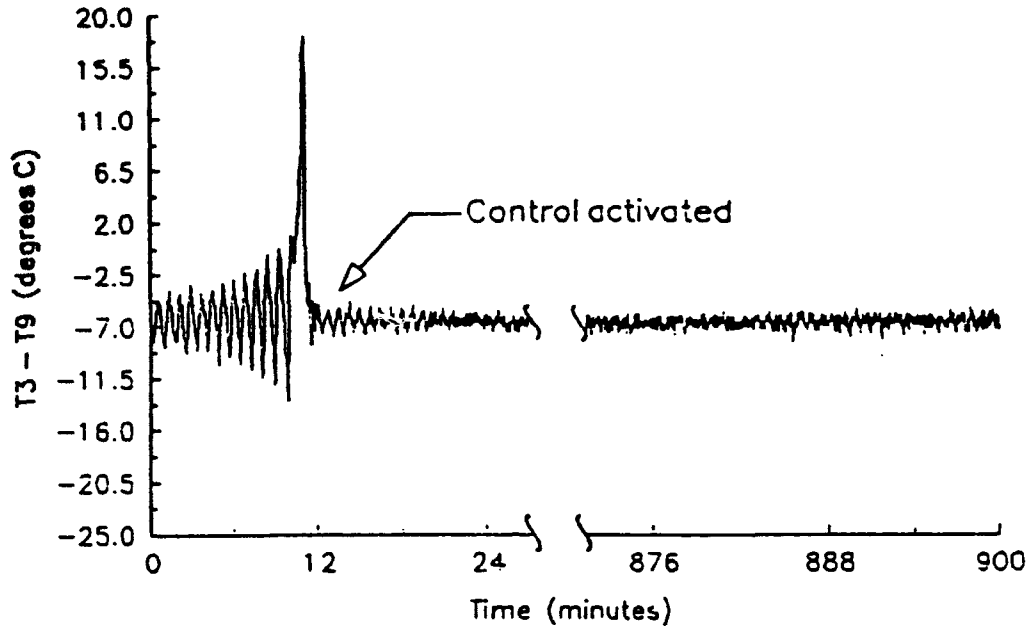
Figure 1: Experimentally Obtained Temperature Difference Versus Time for a Convection Loop [Ref. 2]

temperature mo;..toring system to the heater, the chaotic region could be stabilized. Figure 1 above shows the experimental temperature difference plotted against time. The first 12 minutes show the chaotic behavior, at 12 minutes the control system was turned on and stabilization of the convection loop obtained. This example gives a flavor for the type of Chaotic control that is possible.

1.3 APPLICATIONS AND PROBLEMS

There has been a great amount of interest in the development of an all solid-state laser operating in the blue-green spectrum. The most interesting property of this wavelength region is its excellent transmission in water. As Figure 2 shows, in the visible spectrum there is a peak transmission in the region around 400 nm to 500 nm which can be used for many underwater applications. Other important applications for this wavelength region include; optical data storage, retrographics and image processing.

Most of the lasers that operate in the region of 400 nm to 600 nm are outlined in Table 1. A majority of these lasers are large, costly, use harmful chemicals and require considerable maintenance. Of these options the frequency doubling of a diode laser and a Ti:Sapphire laser seems to hold the most promise.

2
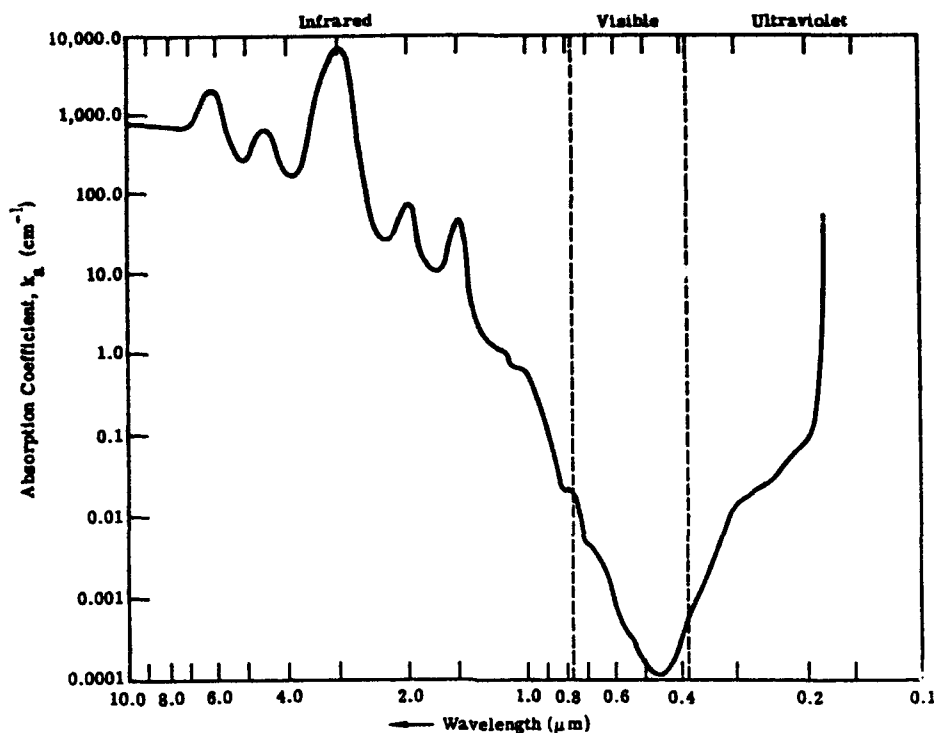
Figure 2: Absorption of Radiation by See Water [Ref. 3]

There has been considerable work conducted in the area of frequency doubling of diode lasers in the past years, and of this work the external resonant cavity doubling exhibits the most potential. In external resonate cavity doubling, the nonlinear crystal is placed inside a cavity that resonates the pump radiation and passes the generated doubled signal. Large conversion efficiencies have been reported [ref. 4] using this technique for doubling of cw diodes. The major problem encountered in using this method of doubling is stabilizing the doubled output. Many elaborate schemes have been developed to solve this problem, which in themselves cause problems.

The problem with instabilities associated with frequency conversion was first observed by Baer [ref. 5]. He observed large scale random intensity fluctuations in the green output of a Nd:YAG laser with an intracavity KTP crystal. James et al [ref. 6] published theoretical and experimental results that exploited the nonlinear dynamics for certain parameter values of the rotatory alignment of the KTP crystal to eliminate the chaotic behavior. They showed theoretically that a stable configuration exists for any given birefringence of the YAG crystal and experimentally illustrated ranges of stable and unstable behavior for a typical cavity configuration and operation conditions. The critical element of the analysis presented by this group was that the YAG rod could be birefringent.

TABLE 1. SUMMARY OF BLUE-GREEN LASERS

TYPE OF LASER	WAVELENGTH (nm)	STATUS
Frequency-doubled Nd:YAG	532	State-of-the-art hydrographic laser; 2 mJ, 400 Hz, 5 nsec device under development
Injection-laser-pumped Nd:YAG	532	Very long life, 5% efficiency; compact configuration possible
Metallic copper	511-578	6 kHz, 0.8 mJ/pulse, 20 ns pulse length available; 8 kHz, 0.7 mJ/pulse, 5 ns pulse length demonstrated
Copper halide	511-578	Demonstrated performance similar to metalic Cu; lower temp. requirement; potential for long-life sealed off Nd:YAG
Mercury bromide	490-510	1 mJ/cm3/pulse, 50 ns operation demonstrated at 100 Hz; long sealed-off life possible; 5 ns pulses possible via cavity dump; 8 ns demonstrated
Mercury chloride	555-565	Same potential as mercury bromide, but long wavelength
Raman down-shifed XeCl	Selectable via Raman medium	Highly developed; 210 W average demonstrated in Vu; 50 donw-conversion efficiency achieved with lead vapor
UV-pumped dye	Tunable in green	Demonstrated using KrF and XeF pumps; requires short-pulse UV pump development
XeF-laser-pumped Tm:YLF	452	Demonstrated in lab; 60% efficiency possible
XeCl-laser-pumped Xe$_2$Cl	478	Demonstrated in laboratory
Cadmium sulfide	495-501	Low-energy operation demonstrated using both optical and electron-beam pumping
Ce:LaAlO$_3$	Tunable in green	Theoretically promising; crystal-growth experiments underway
Frequency-doubled diode array	Green	Very long life; 10% efficiency appears possible; 3 ns pulse length no problem; experiments to phase-lock many diodes underway

The above technique was successfully implemented by Marshall et al [ref. 7] at Fibertek to stabilize a mode-locked diode pumped solid state laser system. The stabilization was achieved by using a feedback loop to control the diode current. They also operated the in cw mode and found large instabilities. But, by using the appropriate rotational alignment of the KTP crystal about the axis of beam propagation they showed the output could be stabilized (see Figure 3).
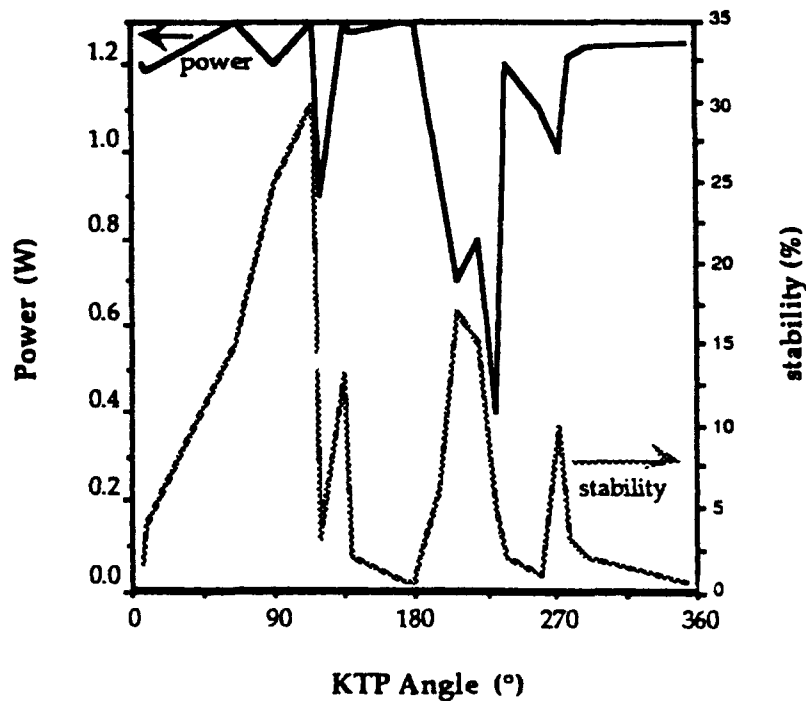
Figure 3: Dependence of Stability and Output Power on KTP Axial Rotations [Ref. 8]

New products that can be used as control elements in laser systems is just one benefit of this type of research. Knowing the stability range of known optical configurations and their component structures by simply controlling the operating system parameters is invaluable for optical communication, spectroscopy, information processing , medical applications, and laser radar. Dynamical control and predictability can be achieved by understanding the nonlinear nature of individual devices and there interaction with light whether they act alone or in concert.

5

2.0 WORK PLAN AND EXPERIMENTAL SET-UP

2.1 PHASE I TECHNICAL OBJECTIVES

The technical objectives for this program as outlined in the proposal were as follows:

1) A literature search of recent work in the area of SHG and its stability improvements.

2) Construction of a bread-broad external resonate cavity with $KNbO_3$ nonlinear crystal.

3) A computer model of the above laser system to understand the parameters which control stability.

4) Provide the most practical means of stabilizing the laser system.

5) Write a Phase II proposal outlining the method for optimization of the Phase I system for maximum long term stability and performance.

2.2 LITERATURE SEARCH

SEO conducted a literature search using computer data bases. For the literature search, the following key words were used:

1) Nonlinear Systems,
2) Second Harmonics Generation,
3) Optical Chaos,
4) Optical Instability,
5) Laser Stability,
6) Dynamical Control,
7) Laser Feedback and Seeding.
8) Chaos Analysis

It may be noted that the published literature on the above topics was found to be abundant. However, the purpose of the literature search was to study the methods to improve stability of the frequency doubled solid state laser used by other research workers and avoid duplication of the effort. A brief summary of the literature collected is provided in Appendix A. Also, the appendix provides some of the important abstracts obtained using the computer search of the data bases. The material collected in this literature search was extensive and it is possible that the collection of all technical papers and scientific reports will provide a reference book on this topic.

2.3 PUMP LASER

SEO selected two types of lasers during this the phase I program as pump sources for an external resonant cavity with a nonlinear crystal $KNbO_3$. (1) Gallium aluminum arsenide (GaAlAs) semiconductor injection laser, and (2) Titanium doped sapphire (Ti:Sapphire) solid state laser. A brief description of each of these lasers is provided below.

a) Gallium Aluminum Arsenide Semiconductor Laser

Four major types of high power single mode (single frequency) devices can be fabricated: (a) Constricted Double Heterojunction, Large Optical Cavity or CDH-LOC (ref. 9), (b) Channel Substrate Planer or CSP (ref. 10), (c) Crank-type Transverse Junction Stripe or Crank-TJS (ref. 11), and (d) Buried Heterojunction, Large optical Cavity or BH-LOC (ref. 12). Such devices have been shown to operate single mode, CW to at least 10 mW/facet. A complete discussion of these devices can be found in a technical paper published by RCA engineers (ref. 13).

For the pulse operation, the CW device will require modulation. A modulated CW diode does not provide a high peak power necessary for some applications. SEO plans to use the stabilized blue-green (430 nm) laser in its laser imaging radar system (see Appendix B) which requires a high peak power (typically 100 W peak for 300 m range).

The pump source of choice is a single frequency GaAlAs semiconductor laser diode operating at 860 nm. A single frequency pulsed diode laser is not available at this time. Therefore, for these experiments a pulsed diode operating at 860 nm, model CVD-97, manufactured by Laser Diode, Inc. New Brunswick, NJ. was selected. The diode can be operated at a high repetition rate (10 KHz) and a narrow pulse width (20 ns). Also, the diode provides a high peak power of 25 W.

b) Titanium Doped Sapphire Solid State Laser

A titanium doped sapphire (Ti:Sapphire), model **Titan-CW** manufactured SEO was selected for its high power (800 mW) and tunability (700 - 1130 nm). An optical schematic and a brief description of the laser is provided in Figure 4. In addition to the high power, the laser provides two separate resonator options. The standing wave resonator provides multi-frequency (2-4 GHz) operation while the ring resonator operates at less than 10 MHz linewidth. Since, the laser diode selected was not the single frequency device, we used a standing wave resonator configuration for these experiments. The Ti:Sapphire laser was tuned to 860 nm wavelength using a birefringent filter. Although, the laser provided 800 mW output power only about 200 mW was used for pumping the doubler. In Figure 5, a photograph shows experimental set-up, Ti:Sapphire laser (front right) pumping the external resonant cavity of $KNbO_3$ (front left) and the argon-ion laser pumping the Ti:Sapphire resonator.

7

Two Lasers In One

The **Titan-CW** is the first Ti:sapphire laser to provide single-frequency ring (10 MHz short-term linewidth), unidirectional ring cavity or multi-frequency (2-40 GHz span) standing wave cavity operation from the same laser. This is due to the **Swing Resonator** (US patent #5,029,179). Changing from a standing wave to a ring cavity is accomplished by a simple rotation of the two flat mirror mounts and the addition of the optical diode, and the procedure is easily reversed. There is no need for the addition of extra mirrors or complicated realignment to switch from one to the other. If your experimental needs change, the Titan-CW laser with the **Swing Resonator** can change with them.

Ring

All **Titan-CW** lasers ordered with the ring-cavity configuration are supplied with Super Invar resonator bases for maximum frequency stability against changes in room temperature. The ring laser is also provided with a single solid etalon for fine tuning. Due to the inherent stability of the solid state gain medium, the linewidth jitter of the **Titan-CW** ring laser is comparable to that of other "stabilized" systems.

The **Titan-CW** also contains a special Ti:sapphire Optical Diode (TOD), unique to SEO. The TOD establishes unidirectional operation of the ring cavity and, unlike other systems, has been designed and built specifically to cover the Ti:sapphire tuning range, providing maximum rejection of the unwanted direction of the ring-cavity oscillation out to long wavelengths. As a result of SEO's continuing dedication and expertise in advancing the performance capabilities of Ti:sapphire, we have demonstrated unidirectional operation out to 1090 nm with a 10 W pump laser. Only the **Titan-CW** is designed to give you the maximum performance in a Ti:sapphire ring laser.
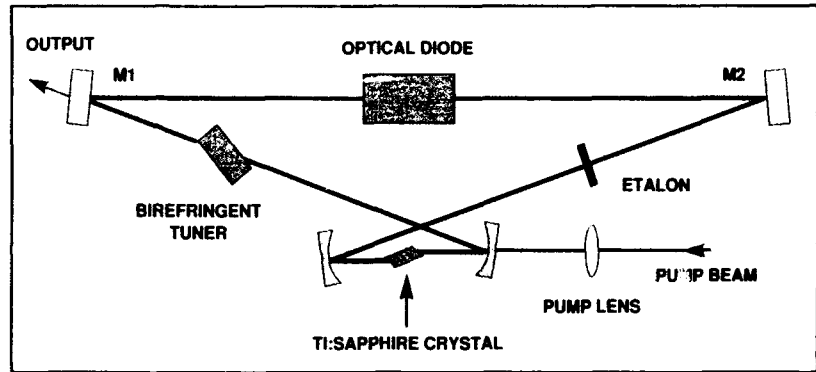
Standing Wave

A **Titan-CW** laser ordered with the standing-wave cavity features a stainless steel resonator breadboard base, but can be optionally supplied with a Super Invar base if frequency-stable ring laser operation is anticipated in the future. Another option is a solid etalon, which will reduce the number of longitudinal modes to within a total span of 2 GHz over the entire tuning range. Without the etalon, the number of modes is unpredictable and may cover a span of up to 40 GHz. The standing wave cavity tuning range is 685-1130 nm with a 10 W pump laser, with somewhat reduced tuning for lower powered pumps.
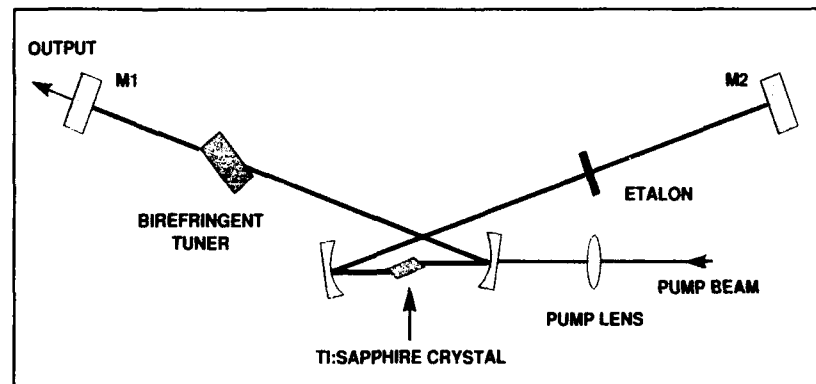
Figure 4: Ti:Sapphire Pump Laser Resonator

8

Figure 5: Photograph of Ti:Sapphire Pumping External Resonant Cavity

2.4 RESONANT CAVITY WITH KNbO$_3$

The external resonant cavity consists of two concave mirrors (M1 and M2) and the KNbO$_3$ crystal. The mirrors were coated for optimized performance in the frequency doubling, and pump resonator line. The input mirror M1 for the pump beam was coated for maximum transmission (T) at 860 nm and a maximum reflectivity (R) at 430 nm. However, the mirror provided 1 % R at 860 nm. The output mirror M2 for the frequency doubled beam was coated for a maximum reflectivity at 860 nm and a maximum transmission at 430 nm. The mirror provided 1 % R at 430 nm. A confocal resonator with a 10 cm radius of curvature was selected for these experiments. The confocal resonator is considered a version of the ring resonator and results in an increased resonant cavity length. The confocal resonator geometry is illustrated in Figure 6. SEO has used this resonator approach for its diode pumped single frequency Nd:YAG lasers. It may be noted that the external resonator provides a frequency doubled output at 430 nm from mirror M2, and a continuous feedback back to the pump laser resonator at 860 nm from mirror M1.

The KNbO$_3$ was placed at the center of the resonator (see Figure 7). KNbO$_3$ is an excellent crystal for doubling of the diode radiation. It possesses nonlinear optical properties that exceed other crystals that could be used. The KNbO$_3$ nonlinear crystal was A-cut for SHG of 860 nm at room temperature in order to take advantage of the noncritical phase-matching condition. The temperature tuning data for a 90° phase matching is shown in Figure 8. This 3 x 3 x 8 mm crystal was grown, cut and AR coated for 860 and 430 nm by Virgo Optics, Port Richey, FL.

Figure 6: The confocal Resonator with the KNbO_3 Crystal

M2

FREQ.
DOUBLED
BEAM

MICROMETER FOR
CRYSTAL AXIS ROTATION

M1

FOCUSING LENS

PUMP BEAM
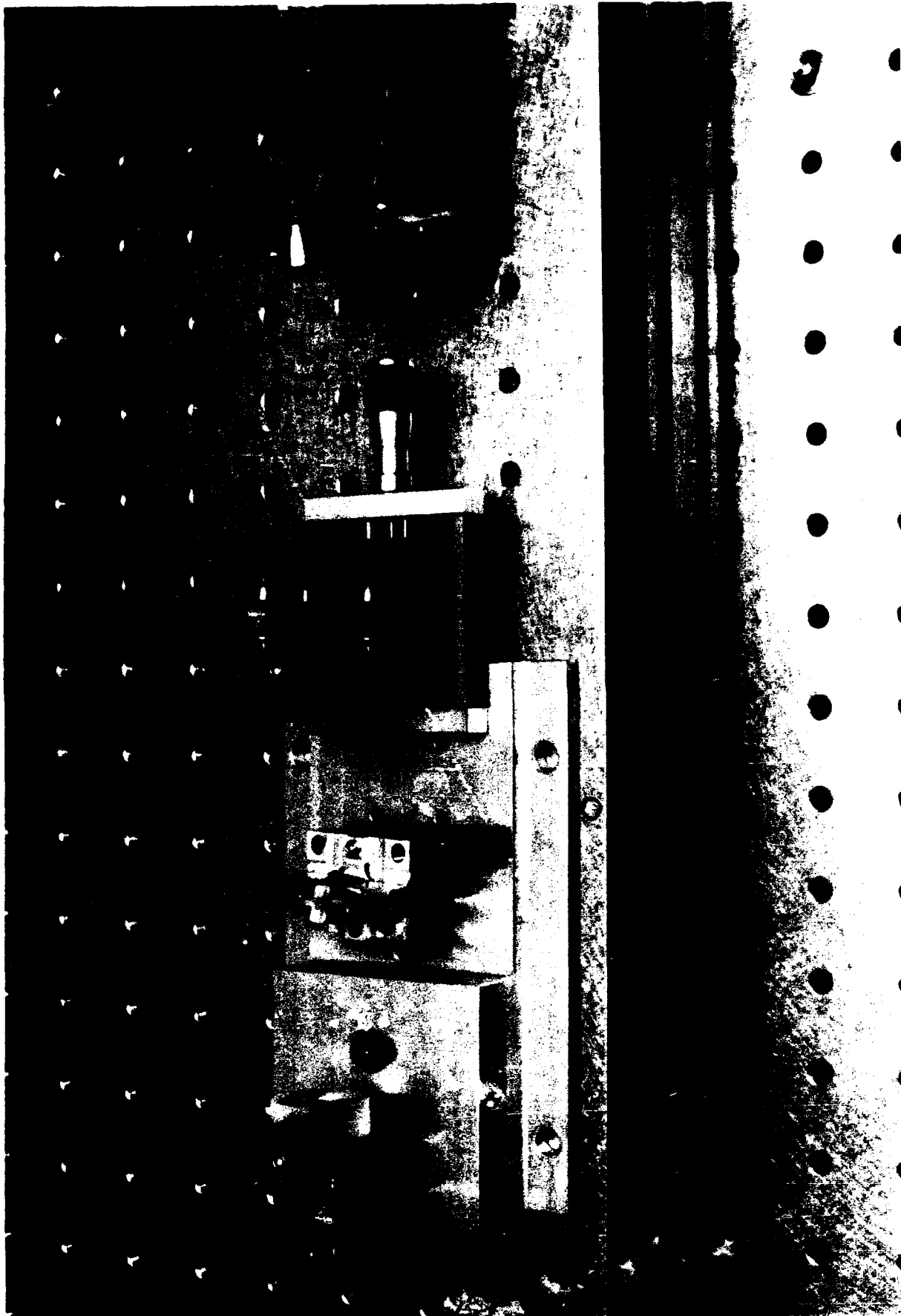
Figure 7: A Photograph of the Resonant Cavity Pumped with the Laser Diode

KNbO$_3$ CRYSTAL

a. properties:
- Orthorhombic, biaxial, mm2 symmetry(for T=-50° C to 223° C).
- Transaprency ranges (micron): 0.4 - 5.0
- Nonlinear coefficient (in pm/V):

$$d_{31} = 15.8 \quad \text{(36 times of } d_{36} \text{of KDP)}$$

$$d_{32} = 20.5 \quad \text{(47 times of } " \quad " \quad " \text{)}$$

- Acceptance widths: (for 90° phase-matched SHG of 860 nm)
  angular: 30 mrad-cm$^{\frac{1}{2}}$, spectral: 0.57 Å-cm$^{\frac{1}{2}}$
  temperature: 0.043°C (for 188°C), 0.5°C(for ~23°C).

b. applications:

- A-cut: for SHG of 840-950 nm (T= ~30°C ~ 200°C)

- B-cut: for SHG of 970-1064 nm (as above temp.)

where: 90° phase-matching available at room temperature
for SHG of 860 nm(using d$_{32}$) & SHG of 986 nm (d$_{31}$).
At 22°C, SHG of 1064 nm matched at angle-cut of 46°.

FIG. 1 Temperature tuning curves for 90° phase-matching
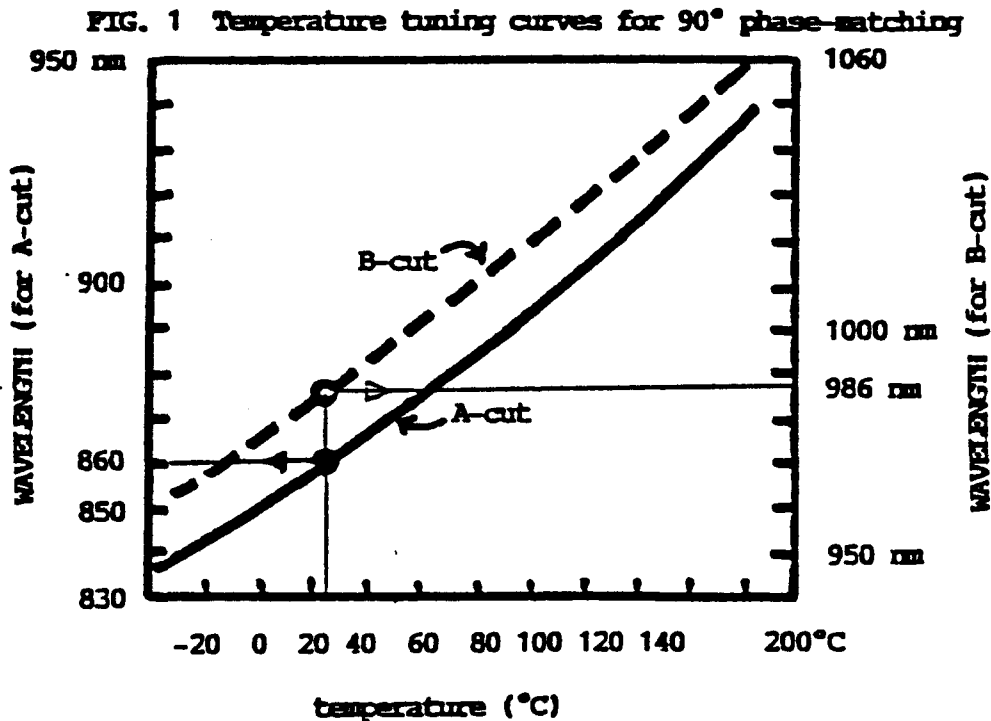
Figure 8. Properties of KNbO$_3$ Crystal [Ref. 14]

3.0   RESULTS AND ANALYSIS

3.1   PUMP LASER CHARACTERISTICS

As discussed in Section 2.0, two types of lasers were selected as pump sources. The performance characteristics of each of the laser following two lasers are briefly given in this section.

a)   GaAlAs Pulsed Laser Diode,

b)   Ti:Sapphire CW Laser.

a)   GaAlAs Pulsed Laser Diode Characteristics

A laser diagnostics set-up used for obtaining the GaAlAs pulsed laser diode characteristics is shown in Figure 9. The laser diode can be wavelength tuned over a wide frequency range by controlling its temperature. Therefore, the diode was mounted on a heat-sink which was cooled/heated using a thermo-electric (TE) cooler. Initially, the external resonant cavity with the $KNbO_3$ crystal was removed in order to obtain the diode laser characteristics.

The laser diode spectral characteristics were obtained using a computer controlled a model 640 monochromator, manufactured by ISA Instruments, Division of Jobin-Yvon, France. The data obtained is plotted in Figure 10. As seen in the figure a FWHM line width of the laser is 2.5 nm.

The output energy and the temporal pulsewidth of the laser was measured using a model RM-6600 radiometer, manufactured by Laser Precision Corp., Utica, NY. The pulse width of the output is shown in Figure 11. It may be noted that the laser diode output pulse width generally follows the pulsewidth of the current pulse which drives the diode. Thus, the diode output pulsewidth can be adjusted from 10 to 50 ns by adjusting the drive current pulsewidth. However, a longer pulsewidth provides more energy and a shorter pulsewidth provides a higher peak power.

As noted before, the diode was selected for its output wavelength and its high peak power. The data collected using the diode shows that the peak power of the diode was 25 W.

b)   Ti:Sapphire CW Laser Characteristics

Since, SEO manufactures and markets this Ti:Sapphire laser, it was possible to use this laser with no cost to the program. Secondly, the complete characteristics for this laser was also available. The laser provided typically 800 mW of continuous wave (CW) output power tunable in tunable range of 700 to 1130 nm.

14
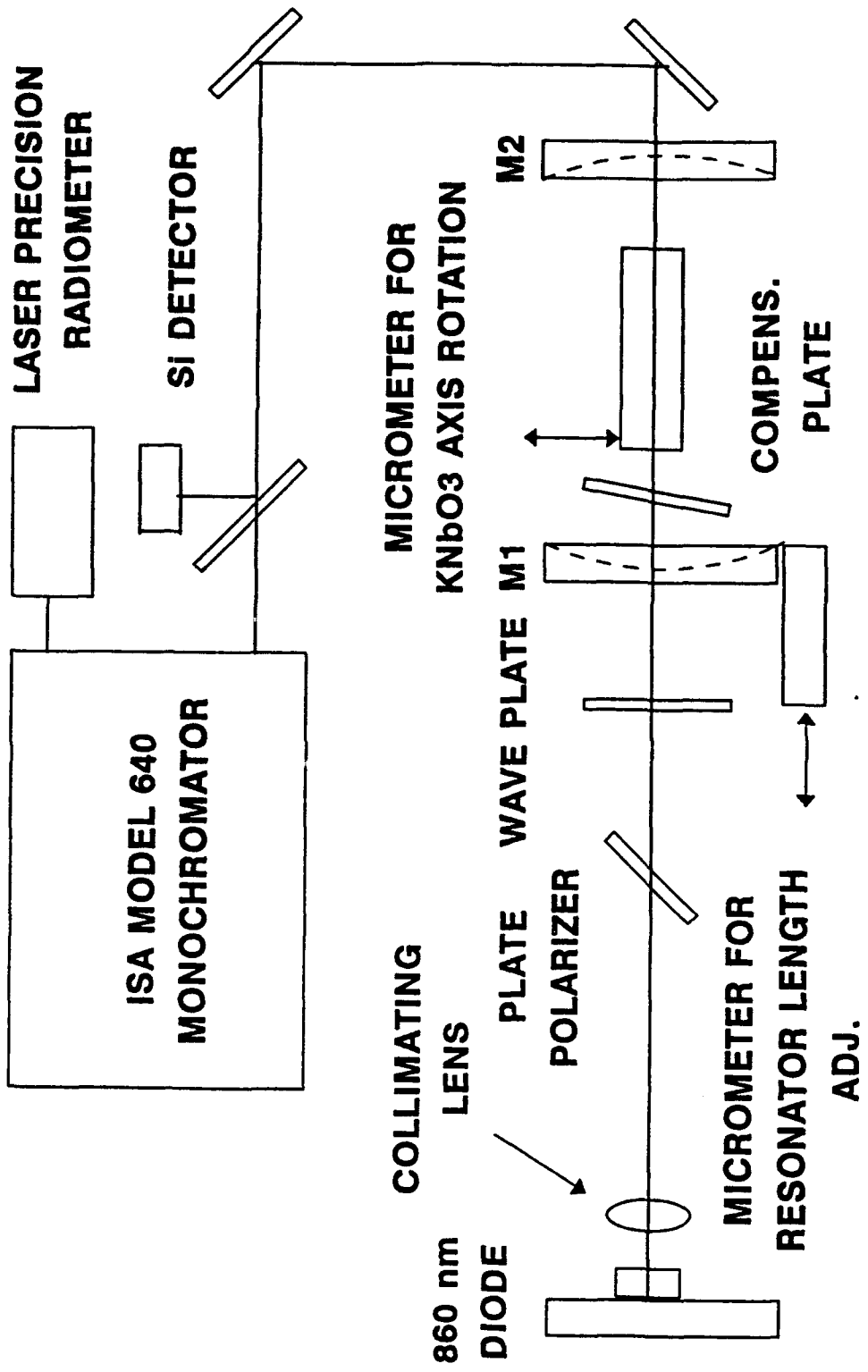
Figure 9: Laser Diagnostics Set-Up for the GaAlAs Laser Diode
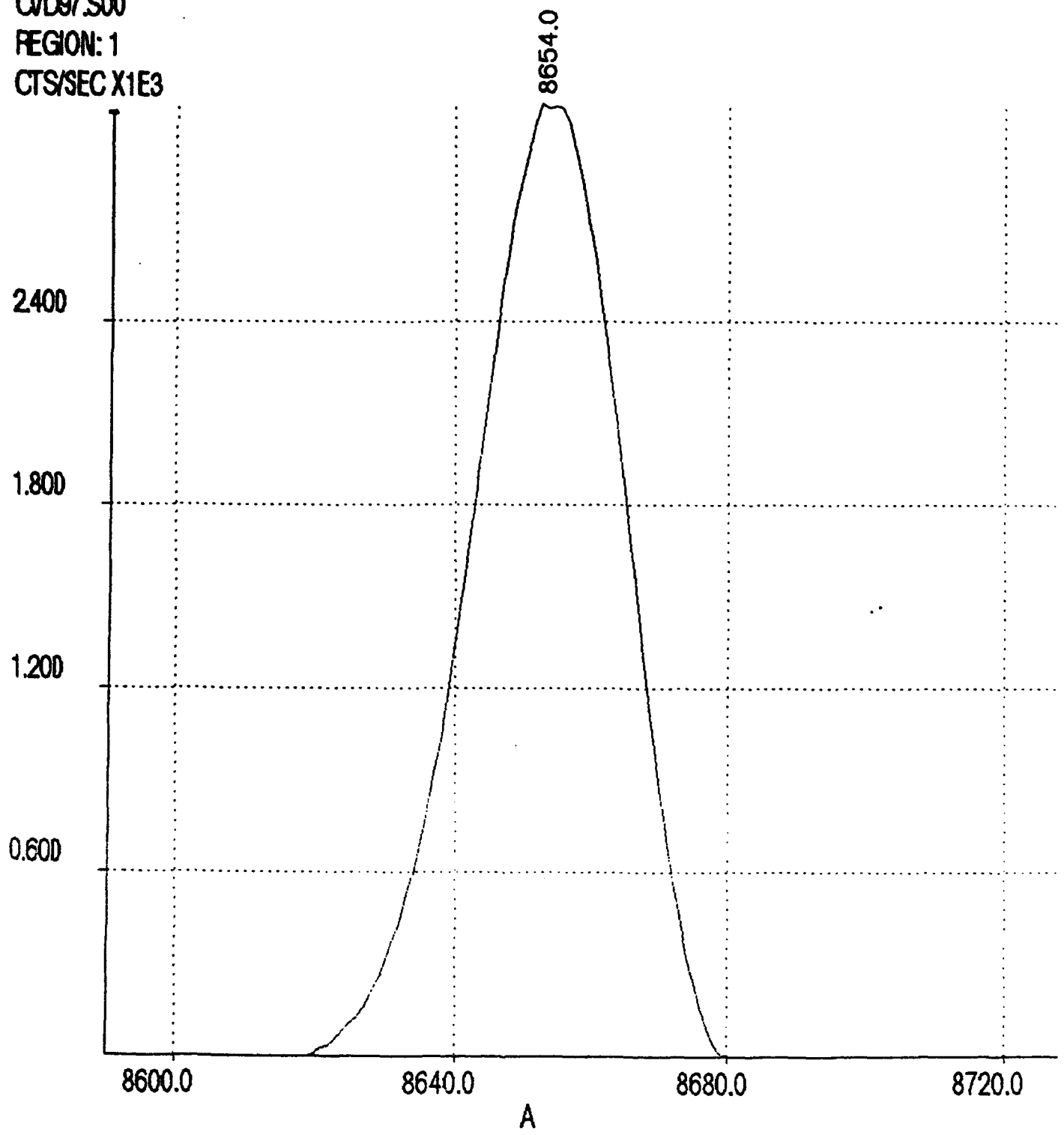
Figure 10: Spectral Characteristics of the GaAlAs Laser Diode Output

16
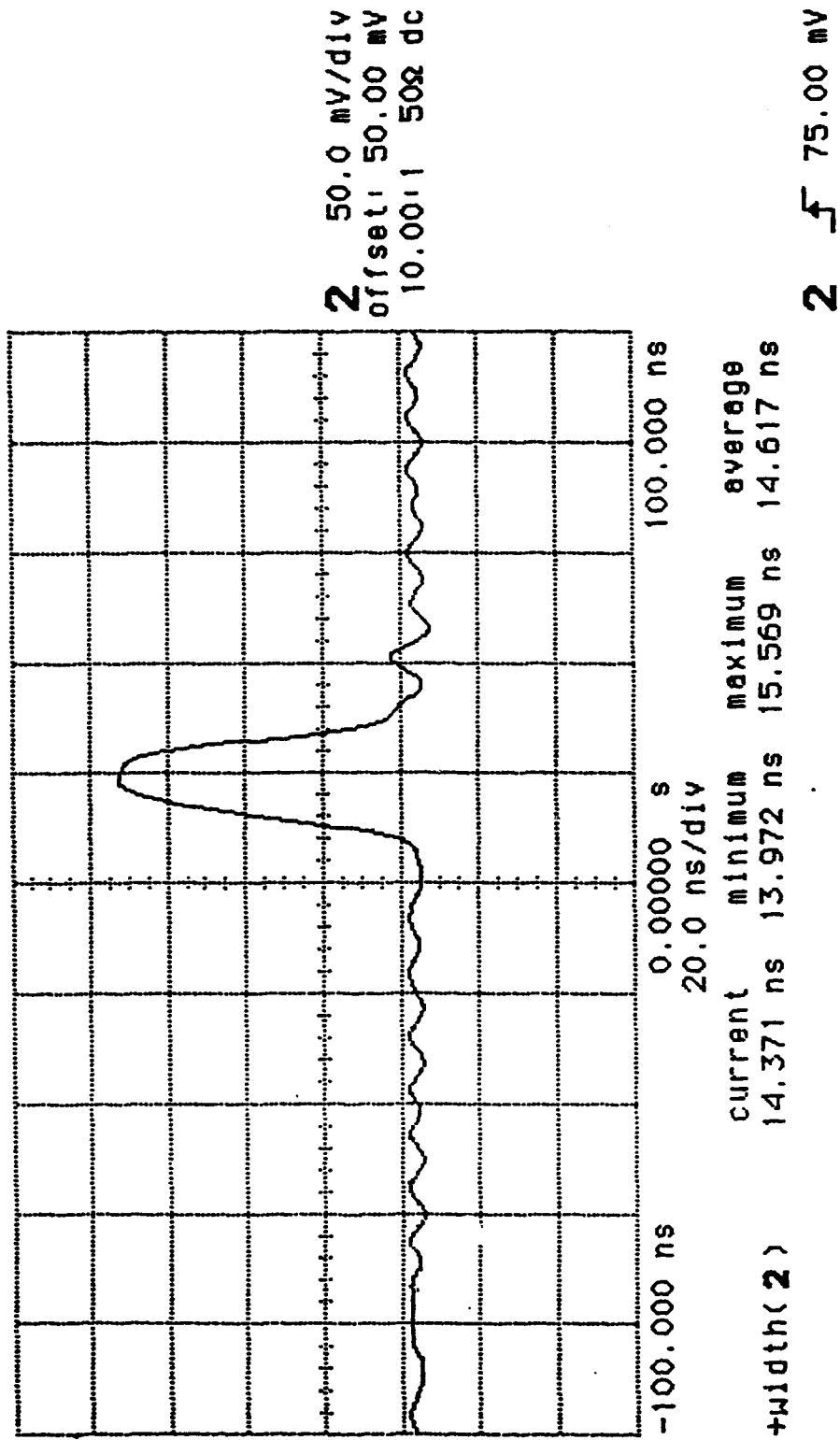
Figure 11: Temporal Characteristics of the GaAlAs Laser Diode Output

17

Although, the complete Ti:Sapphire laser characteristics were available, the laser diagnostics set-up as shown in Figure 12 was used to monitor critical laser parameters. The laser wavelength tuning was obtained with the birefringent tuner in conjunction with a model Wavemeter Junior, manufactured by Burleigh Instruments, Inc., Fisher, NY. Once the laser was tuned to provide 860.00 nm wavelength, the linewidth and mode separation measurements were performed. Before measuring the linewidth and mode separation for the Ti:Sapphire laser, the external resonant cavity was removed from the set-up. For the linewidth measurements a confocal etalon spectrum analyzer model RC-46, manufactured by Burleigh Instruments, Inc. The typical linewidth data obtained for the laser is provided in Figure 13. The data collected indicated that the line width of 3 GHz.

3.2 STABILITY OF FREQUENCY DOUBLED OUTPUT

The external confocal resonant cavity with the $KNbO_3$ was aligned using the pump laser for alignment. The $KNbO_3$ crystal rotation plays a critical role in obtaining a high conversion efficiency of SHG. The crystal was mounted on a turn table to allow this crystal rotation. The over all size of this confocal resonant cavity was very small, the mirror M_1 and M_2 were separated 10 cm. The base plate for the mirror mounts and the turn table with $KNbO_3$ were packaged in a 15 x 5 x 5 cm housing. A color photograph in Figure 14 illustrates the performance of the resonant cavity.

The variation of the output intensity of a resonant cavity can be obtained using the resonance spectrum characteristics (ref. 15). The frequency spacing of the longitudinal modes δv = c/2l, where l is the mirror separation of the resonator. Hence, the resonant cavity will oscillate in a number of frequencies separated by c/2l and the total numbers of oscillating modes will be given by:

$$\text{Number of oscillating modes } N = \frac{\Delta v}{c/2l}$$

The total output of the resonator is a superposition of the fields of all modes, and output intensity is proportional to $| E(z, t) |^2$.

Thus intensity, $I(t) = K | E(t) |^2$

Where K represents a proportional constant

For arbitrary values of the amplitude and phase of the various modes, the output intensity of this resonator will fluctuate showing chaotic behavior. Thus, the simple method to improve the resonator stability of this external resonant resonator is to pump it with a single frequency laser.

18
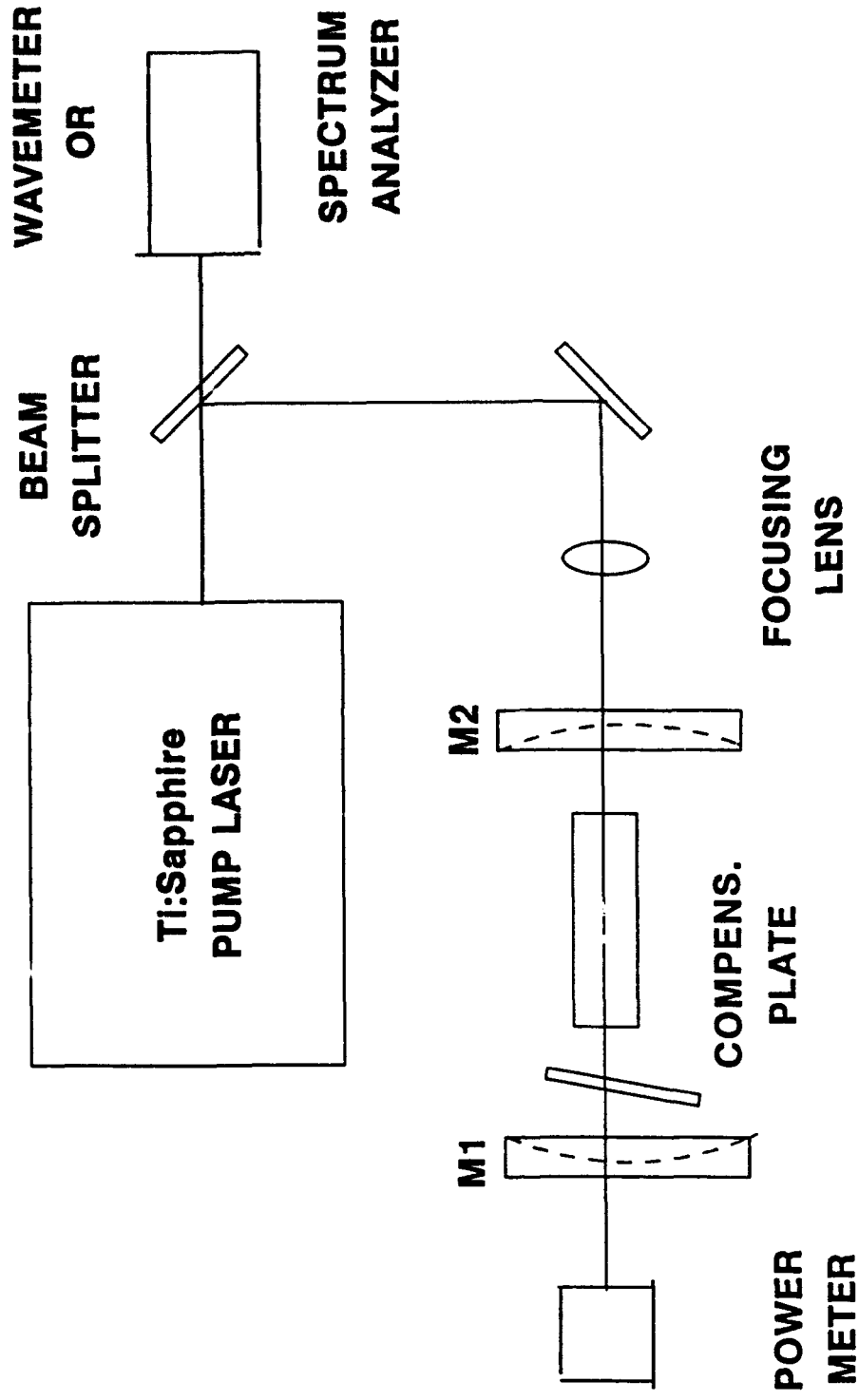
Figure 12: Laser Diagnostics Set-Up for Ti:Sapphire Laser

19

TEK/2480

CH2   DC   2 V /div   NORMAL   1mSEC/div   CH2

T

CH2 +
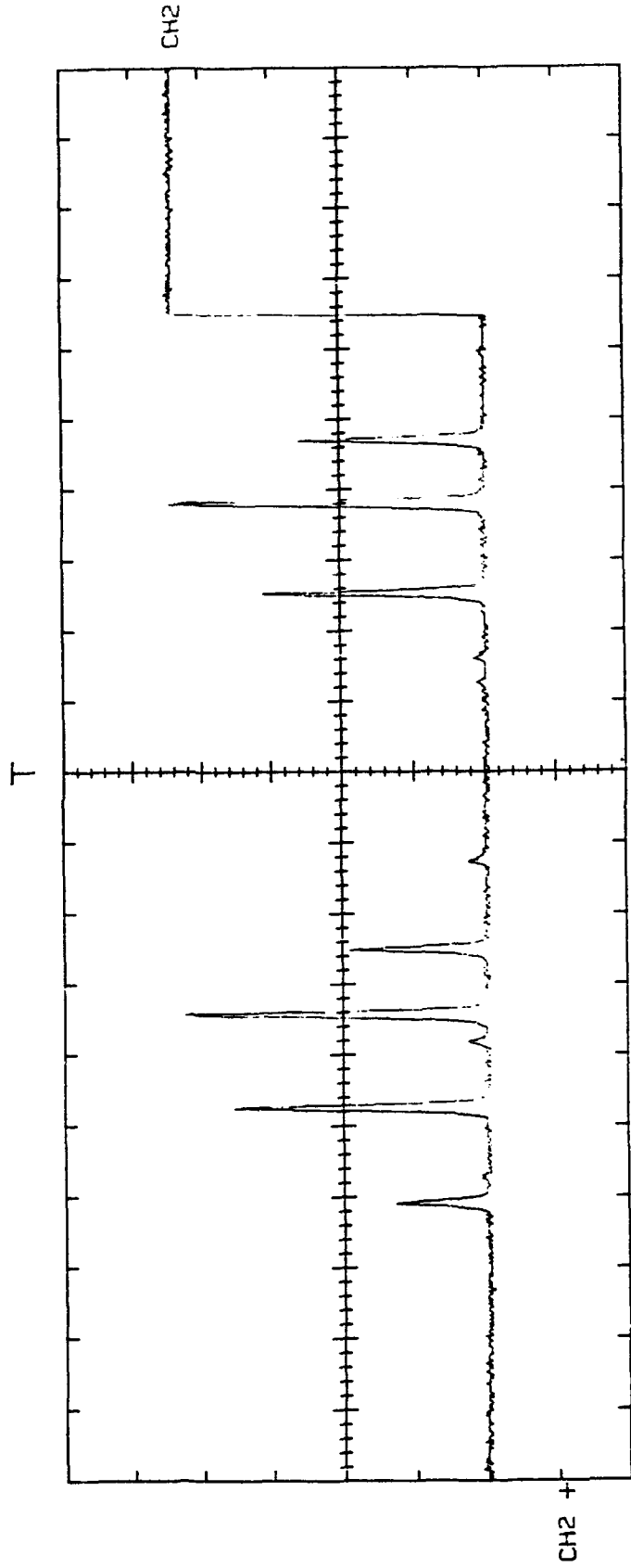
Figure 13: Laser Linewidth of 3 GHz for the Pump Laser Without Feedback
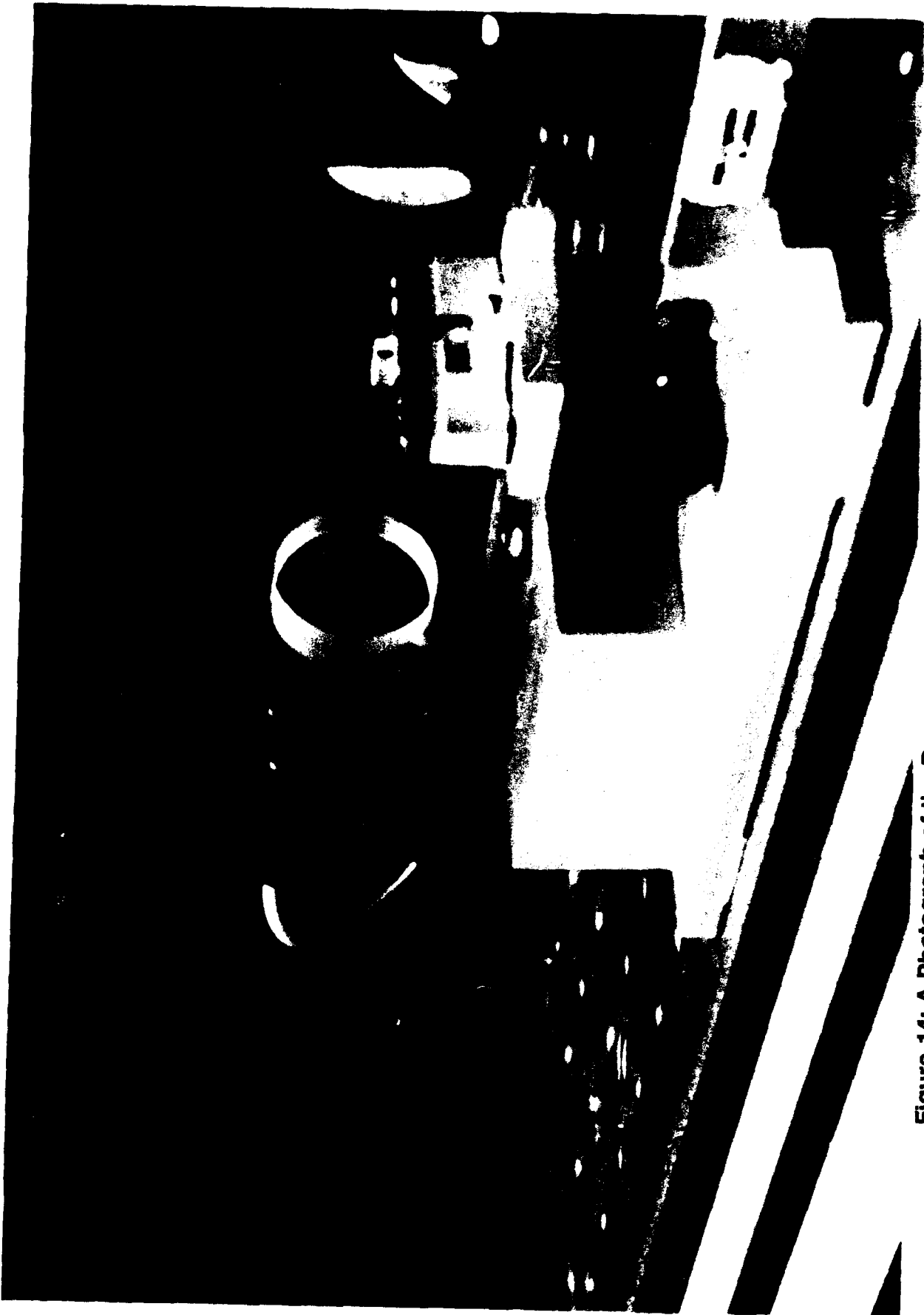
Figure 14: A Photograph of the Resonant Cavity showing Frequency Doubled Output of 860 nm at 430 nm

The amplitude of the resonant cavity output at 430 nm was monitored by using a silicon detector model DET-1, manufactured by Thorlabs, Inc., Newton, NJ. The output of the detector output was recorded on Tektronix 2440 oscilloscope. The data obtained is plotted on Figure 15. This poor stability of the doubled output is due to the multimode operation of the pump laser.

3.3 CONTINUOUS FEEDBACK TECHNIQUE

A simple method to improve the intensity stability of the external laser is to reduce the pump laser linewidth. SEO offers **Titan-CW** laser with an etalon in a ring resonator with a Faraday rotator to obtain only unidirectional oscillations in the resonator. This approach was not possible since it was not feasible for the pulsed laser diode.

The external confocal resonator with the $KNbO_3$ crystal is the passive resonator for the pump laser frequency. Generally, an isolator is used between the pump laser and the external resonator. However, we used a compensator plate in this external resonator and provided a feedback into the pump laser to reduce the oscillating modes in the Ti:Sapphire laser. For the confocal resonator at 860 nm, the longitudinal mode separation can be obtained by:

$$\Delta \lambda_p \quad = \quad \lambda_0^2 / 4 \ l$$

Where λ_0 =   860 nm,

and l =   10 cm

Therefore, $\Delta \lambda_p$ =   1.849 x 10^{-4} nm.

The line width of the a single longitudinal mode separation can be derived using relation given below:

$$\delta \lambda \quad = \quad \frac{\lambda^2 \ [\ 1 - (\ R_1 \ R_2 \ )^{1/2} \ ]}{4 \ l \ \pi \ (\ R_1 \ R_2 \ )^{1/2}}$$

Where R_1 & R_2 are the confocal resonator reflectivities at 860 nm, as given in section 2.4 of this report:

R_1 =   1, and

R_2 =   0.01

TEK/2430

CH1   DC   5 V /div   NORMAL   500mSEC/div

CH1

T

CH1
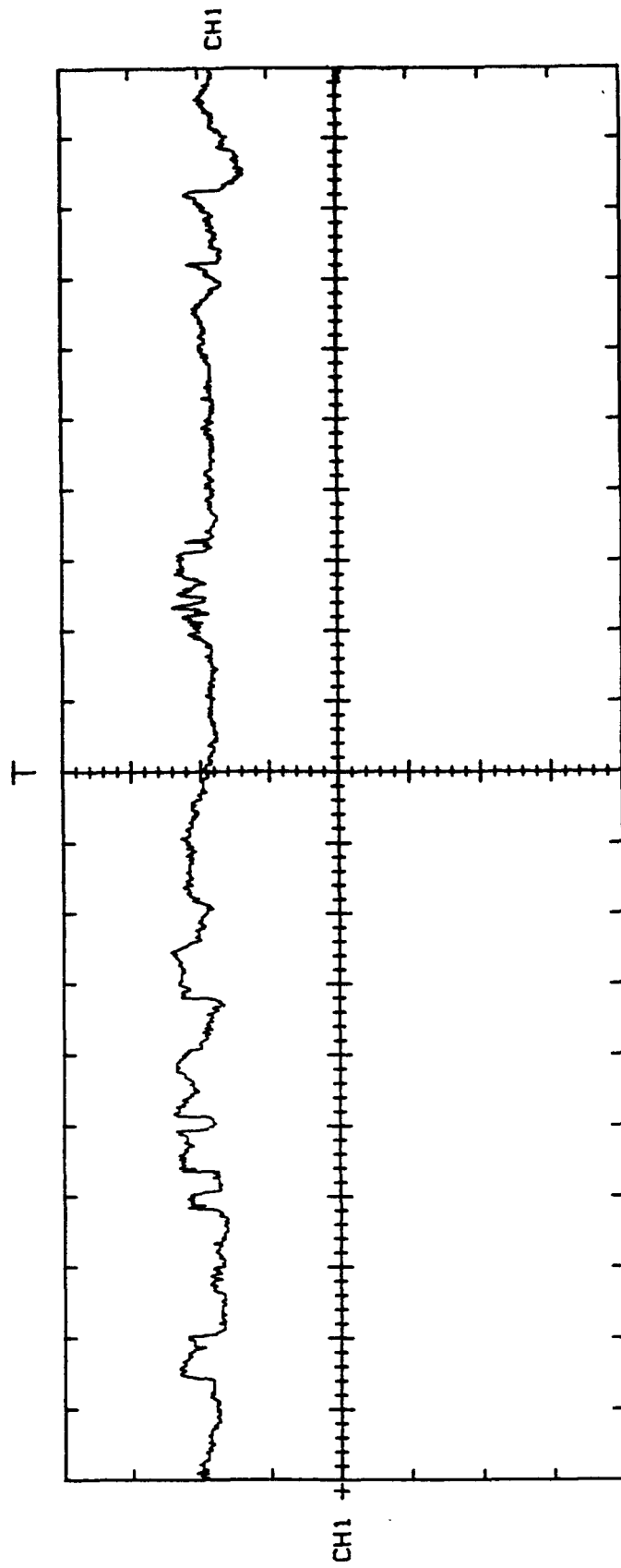
Figure 15: Amplitude Stability of 430 nm Output Without Feedback from
the External Resonant Cavity

23

Thus,
$$\delta\lambda = \frac{(860 \times 10^{-9}\ [\ 1 - (\ 0.01\ )^{1/2}]}{4 \times 10 \times 10^{-2} \times \pi\ (\ 0.01\ )^{1/2}}$$

$$= 5.297 \times 10^{-3}\ nm$$

These longitudinal modes in the external confocal laser resonator for 860 nm can be represented as shown in figure 16 below:
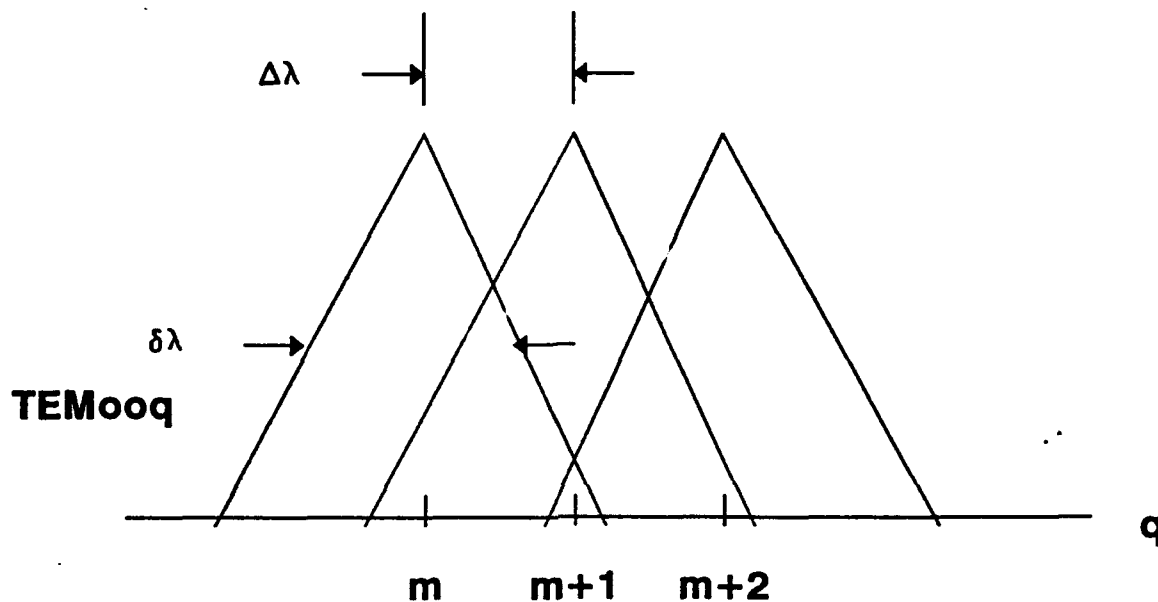
Figure 16: Longitudinal Modes in the External Confocal Resonator

A resonance frequency in this external resonator is obtained by inserting a compensator plate with a small tilt and the KNbO$_3$ crystal (ref. 16, 17). The compensator plate tilt is adjusted so that the interferometer path length remains unchanged with the change in wavelength of the pump laser. Thus, a continuous feedback from the external resonator to the pump resonator is possible.

The approach is simple and provides dynamical alignment to the pump laser resonator by feedback from the external resonator. A multi-mode, multi-wavelength pump laser can be used. Only requirement is that the external resonator length must not change with the environmental conditions. This is achieved by matching materials selection and the mechanical design of the external resonator.

The input mirror for the pump beam has a maximum reflectivity at 430 nm and maximum transmission at 860 nm. The measurements of the mirror M1 indicated only 1 % R at 860 nm. Thus, the longitudinal mode selected can be feedback into the pump laser continuously. The rotation of the compensation plate is required one time only. Thus, ɔ amplitude stability for the frequency doubled output at 430 nm can be improved with the correct tilt of the compensation plate. The same result can be obtained by rotating the KNbO$_3$ crystal, however, the crystal rotation improves the stability but reduces the conversion efficiency. It is desirable to rotate the crystal to obtain high conversion efficiency, and the compensation plate for the feedback to achieve single longitudinal mode operation of the pump laser. The linwidth measurements of the pump laser are shown in Figure 17 indicate significant reduction in the pump laser linwidth due to the feedback. The amplitude of the frequency doubled output at 430 nm was again monitored by using the silicon detector model DET-1. The output of the detector was recorded on Tektronix 2440 oscilloscope. The data obtained is plotted on Figure 18. This excellent stability of the doubled output is due to the continuous feedback technique used on the pump laser. The conversion efficiency of greater than 5 % was observed by using the Ti:Sapphire pump laser. The data was collected using the laser diode as the pump source at this time.

The mathematical derivation for the technique outlined above has been given by Sayeh et al (ref. 18, see Appendix C). Three basic differences between the approach outlined in our work may be noted: (a) Sayeh used the external resonator with a conventional ring geometry with four mirrors to provide the continuous feedback as compared to the confocal geometry of the present work. (b) We used the KNbO$_3$ crystal in the external resonator and extracted only the frequency doubled output. This type of frequency doubler was not used by Sayeh. (c) Sayeh used a alignment optics to provided the feedback, in the work presented here only 10 % of 860 nm was converted in to 430 nm and the remaining 860 nm was available for the feedback, thus a critical alignment was necessary in this work.

3.4 NUMERICAL MODEL

SEO with the help of Dr. Bandy's group at Oklahoma State University used the recent techniques of stabilizing nonlinear dynamic systems. Experimental and computer modeling of the external resonant cavity with different stabilizing parameters were studied. The initial objectives was to examine the recent theoretical work in this area, which include simple deterministic rate equation models that describe the fluctuating laser intensity and the recent work by Roy (ref. 19 & 20) which was used as a paradigm for investigation of this of systems. A set of rate equations were constructed that describe the intensity and gain depending on the number of modes of the system. The stability analysis was performed to investigate the dynamical evolution of the system variables. The computer modeling of the laser system was conducted at OSU. At the time this report was generated, the correlation between the experimental data and the model was being evaluated. Some of this data will be used in the Phase II proposal.

TEK/2430

CH2   DC   2 V /div   NORMAL   1mSEC/div
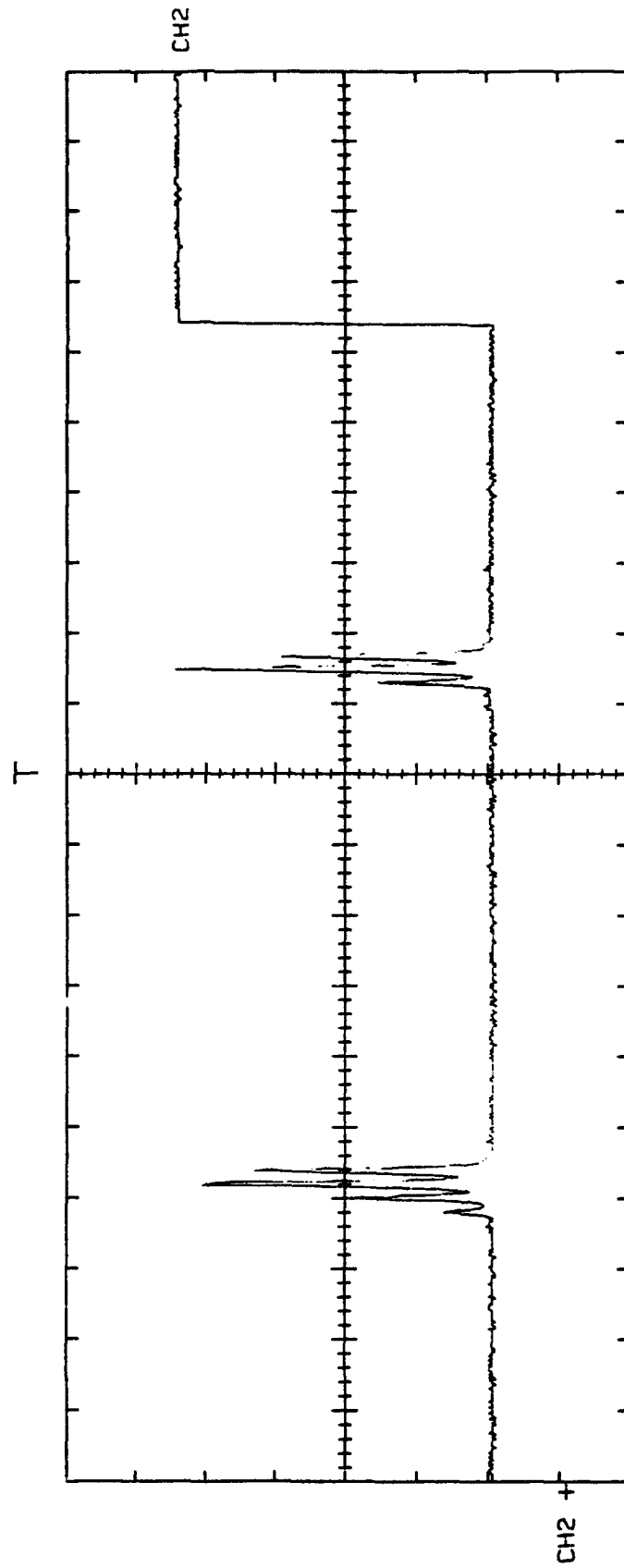
**Figure 17: Laser Linewidth of less than 100 MHz for the Pump Laser
With Feedback from the External Resonant Cavity**

TEK/2430

CH1   DC   5 V /div   NORMAL   500mSEC/div
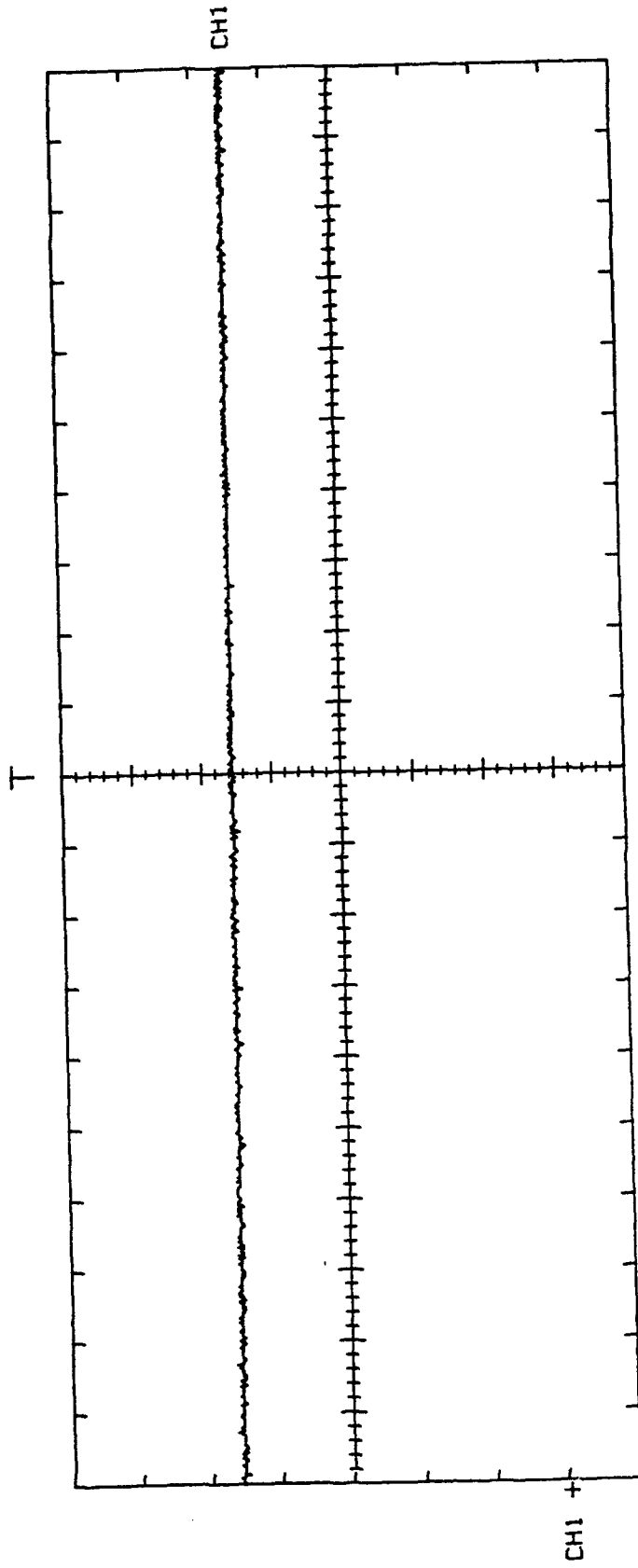
Figure 18: Amplitude Stability of 430 nm Output With Feedback from the External Resonant Cavity

4.0 SUMMARY AND CONCLUSION

4.1 SUMMARY

The work performed in this SBIR Phase is summarized below:

1) Initially, SEO conducted a literature search of recent work in the area of SHG and its stability improvements.

2) We selected a CW tunable Ti:Sapphire laser and a GaAlAs pulsed laser diode operating at 860 nm as the pump sources.

3) SEO constructed an external confocal resonant cavity with a $KNbO_3$ nonlinear crystal for doubling an 860 nm pump laser into a 430 nm stabilized source.

4) The external resonator used a compensation plate for correcting its path length with the pump laser wavelength change. The input mirror of the resonator was dielectric coated for 99 % reflectivity at 430 nm and 1 % reflectivity at 860 nm. The resonator provided continuous feedback to the pump laser.

5) This innovative technique provided the most practical means of stabilizing the frequency doubled output.

6) A computer model of the above laser system was developed to understand the parameters which control stability.

All the goals of this Phase I SBIR program were achieved. The program was completed on schedule and within the program budget.

4.2 CONCLUSIONS

The following conclusions may drawn based on the results obtained during the program:

1) SEO demonstrated an innovative approach of continuous feedback from an external resonant cavity to convert a multimode pump laser operating at 860 nm into a single longitudinal mode laser.

2) The external resonant cavity performed also another important role. It extracted frequency doubled output at 430 nm by using a $KNbO_3$ crystal in the external resonator. This approach is unique and results in a stabilized output at 430 nm.

3) The numerical model developed during the program will allow SEO to scale the system to a higher power blue-green source using laser diode array. The source can be used for the Navy application of Underwater Laser Imaging Radar System (ULIRS).

5.0   PHASE II PROGRAM PLANS

The Phase II project will be to optimize the continuous feedback technique from experimental and computer modeling using the results of this phase I program as a basis. Also, longer wavelength (910 nm) and higher power diodes will be used. A high power laser system capable of a long term stability and an optimum operation suitable for a blue-green imaging radar will be constructed.

New products that can be used as control elements in laser systems is just one benefit of this type of research. Knowing the stability range of known optical configurations and their component structures by simply controlling the operating system parameters is invaluable for optical communication, spectroscopy, information processing , medical applications, and laser radar. Dynamical control and predictability can be achieved by understanding the nonlinear nature of individual devices and there interaction with light whether they act alone or in concert.

In Phase II program, the Laser Imaging Radar System (LIRS) SEO has developed (see Appendix B) using GaAlAs laser diode array will be converted to an Underwater Laser Imaging Radar System (ULIRS). The system of this type will be useful in underwater mines detection applications.

6.0 REFERENCES

1. J. Singer, Y-Z Wange, and Haim H. Bau, "Controlling a Chaotic System," Phys. Rev. Lett. **66**, 1123 (1991).
2. J. Singer, Y-Z Wange, and Haim H. Bau, "Controlling a Chaotic System," Phys. Rev. Lett. **66**, 1124 (1991).
3. Infrared Handbook, 3-107.
4. J. Hall, H.J. Kimble, S.F. Pereira, and M. Xiao, Phys. Rev. A, 38, 4931 (1988).
5. T. Baer, J. Opt. Soc. Am. B3, 1175 (1986).
6. G.E. James, E.M. Harrell, C. Bracikowski, K. Wiesenfeld and R. Roy, Opt. Lett., 15 1141 (1990).
7. L.R. Marshall, A.D. Hays, A. Kaz, J. Kasinski and R.L. Burnham, Proceedings on Advanced Solid-State Lasers, 1991, Vol. 10, (G. Dube' and L. Chase Editors), 240.
8. L.R. Marshall, A.D. Hays, A. Kaz, J. Kasinski and R.L. Burnham, Proceedings on Advanced Solid-State Lasers, 1991, Vol. 10, (G. Dube' and L. Chase Editors), 245.
9. D. Botez, Appl. Phys. Lett. 36 (3), 190, (1980).
10. K. Aiki, M. Nakamura, T. Kuroda, J. Umeda, R. Ito, N. Chinone, and M. Maeda, IEEE J. Quantum Electron, QE-14 (2), 89, (1978).
11. H. Kumabe, S. Nita, Y. Seiwa, T. Tanaka, T. Sogo, SHoriuchi, and S. Takamiya, Tech. Digest IEEE/OSA Conf. Lasers and Electro-Optics, CLEO-81, Paper FA4, Washington, D.C. (June 1981).
12. N. Chinone, K. Saito, R. Ito, K. Aiki, and N. Shige, Appl. Phys. Lett. 35 (7), 513, (1979).
13. D. Botez, D.J. Channin, and M. Ettenberg, Optical Eng. 21 (6), 1066, (1982).
14. J.T. Lin, Advances and Applications of New Nonlinear Crystals, SPIE Short Course Notes, p27 (1989).
15. W. Koechner, Solid State Laser Engineering, Springer-Verlag, New York, p. 207, (1976).
16. W.W. Rigrod, "Selectivity of Open Ended Interferometric Resonators," IEEE J. Quantum Electron. QE-6, 9, (1970).
17. P. Bernard, "Fine Frequency Tuning of High Power CO_2 Lasers," Opt. Commun., 37, 285 (1981).
18. M.R. Sayeh, H.R. Bilger, and T. Habib, "Optical Resonator with an External Source: Excitation of the Hermite-Gaussian Modes," Appl. Opt. 24, 3756, (1985).
21. G.E. James, E.M. Harrell and R. Roy, Phys. Rev. A41, 2778 (1990).
22. G.E. James, E.M. Harrell, C. Bracikowski, K. Wiesenfeld and R. Roy, Opt. Lett., 15 1141 (1990).

APPENDIX A

LITERATURE SEARCH

APPENDIX A: LITERATURE SEARCH

The literature search data collected may be divided in following four categories:

a) **Blue-Green Laser Sources:**   Owing to the variety and large number of applications in optical physics, the interest in frequency doubling from the infrared spectral regions to blue green wavelength is rapidly growing.   Frequency doubling permits, for example, the extension of diode laser wavelengths (860 nm for GaAlAs) to the blue-green wavelength (430 nm), spectral region by incorporating a nonlinear material in the system. The applications include optical data storage at potentially real densities of several Gbits/in^2 (ref. 1), the generation of squeezed states of light via the second order susceptibility (ref. 2), and generation of blue-green light for experiments in the low absorption region of water.   The critical issues facing these systems that incorporate nonlinear frequency upconversion are the stability and available pump power or efficiency of operation at the blue-green wavelength.   Extensive theoretical literature is available (ref. 3-10) for modeling these systems.

Although different pump lasers and frequency doubling crystals are used, this review of the theoretical literature stresses $KNbO_3$. $KNbO_3$ is one of the most interesting materials for nonlinear optics applications due to its large electro-optic coefficients (ref. 11), its large nonlinear optical susceptibilities, and.its strong birefringence (ref. 12). The $KNbO_3$ crystal has a large optical nonlinearity that permits noncritical phase matched frequency doubling of diode lasers at room temperature (ref. 13). By coupling the diode laser radiation to a passive resonator that contains the $KNbO_3$ crystal (ref. 14-16), efficient second harmonic generation (SHG) is possible. In general, $KNbO_3$ as a nonlinear frequency upconversion crystal can be configured in the system either as intracavity or an external cavity.

b) **Laser Diode Pumped Nd:YAG with Intracavity KTP:** The first observation of large amplitude fluctuations in a laser diode pumped Nd:YAG (neodymium doped yttrium aluminum garnet) laser with an intracavity KTP (potassium titanyl phosphate) nonlinear crystal was made by Baer (ref. 17). He simultaneously introduced a rate equation theory for a multi longitudinal mode laser oscillator with an intracavity doubling crystal that included term for the sum frequency (I_iI_j dependency) and frequency doubling (I_j^2 dependency) processes. He accurately identified the sum frequency coupling as the nonlinearity which caused destabilization and predicted the dependance of large amplitude fluctuations on the pump level, the nonlinear coupling constant, and the number of oscillating modes.

Without the intracavity KTP crystal, the laser output field was stable, with the intracavity nonlinear crystal inserted, large random looking fluctuations occurred (ref. 17).   Previous theoretical treatments did not find amplitude fluctuations; they assumed single mode (ref. 18-22) or mode locked (ref. 23, 24)

operation of the laser, but did not consider the destabilizing, intracavity sum generation process. Mandel et al. (ref. 25, 26) who analytically and numerically examined the stability of the Baer rate equations and confirmed Baer's report that mode-mode competition significantly altered the nature of the output solutions. James et al. (ref. 27) followed (i) by shoeing that the dynamical amplitude fluctuations were chaotic in origin and (ii) by generalizing the model (ref. 17) to include arbitrary angular settings of a quarter wave plate within the cavity. A problem first resolved by Oka and Kubota (ref. 28) who experimentally demonstrated the stabilization of such a laser through the introduction of a quarter-wave plate into the cavity.

c) **Frequency Doubling with $KNbO_3$:** $KNbO_3$ is an attractive nonlinear crystal because of the large second order susceptibility and nonlinear mixing (ref. 14, 15, 29-32). The following are examples of systems that employ external buildup cavities:

(1) An electronic servo technique, which makes use of the convenient frequency modulation and current tuning capabilities of semiconductor lasers was used to lock the output frequency of a GaAlAs diode laser to a monolithic ring resonator of $KNbO_3$. This resulted in stable (several hours) and efficient SHG of blue 428 nm radiation with a CW output power up to 41 mW providing conversion efficiency of 10 percent (ref. 31).

(2) A 150 mW of power at 467 nm was generated by nonlinear mixing of diode and Nd:YAG lasers in $KNbO_3$ (ref. 32).

(3) Titanium Sapphire ($Ti:Al_2O_3$) laser was used recently for external cavity doubling with $LiIO_3$ to produce 40 mW of broadly tunable blue output light for 600 mW of IR input (ref. 33).

Although research in this area employs external buildup cavities to enhance the conversion efficiencies, the absolute blue power is still very much limited by the available pump power (ref. 2). In this regard, the titanium sapphire laser is an agreeable source since 2 W of single frequency output power is readily achievable (ref. 2). An early theoretical treatment of harmonic output is given by Ashkin et al. (ref. 34) who analyzed SHG in an external resonator.

The following are examples of systems that employ intracavity SHG: For doubling schemes with $KNbO_3$ within the $Ti:Al_2O_3$ laser cavity, 100-150 mW of blue light power near 430 nm has been obtained in unpublished experiments in Kimble Laboratory and the Baer Laboratory. Polzik and Kimble recently improved the intracavity passive losses to a level of 0.8% in a new doubling cavity and have obtained 60 mW of CW blue light for 100 mW or IR input (ref. unavailable - reported in ref. 2).

Recent progress in the diode laser upconversion in bulk nonlinear resonators is presented by Dixon (ref. 35) and Sasaki (ref. 36). The development of compact blue-green laser sources by frequency conversion is being done mainly for high

density optical memories in an experimental environment. Coherent light sources based on intracavity SHC 'aser diode-pumped solid state lasers have been investigated intensively by a number of researches (ref. 37-39). For example: Stable and efficient green light obtained by intracavity frequency doubling of Nd:YVO₄ is reported by Y. Kitaoka it. a. (ref. 40). The Nd:YVO₄ crystal is a promising material for producing a green light source for the high-density optical disk (ref. 41-42) that offers several advantages, such as high-emission cross section and a large absorption coefficient.

Further experimental work is reported on frequency upconversion using fiber lasers (ref. 43) and waveguides doped with $KNbO_3$ and other materials (ref. 44). Theoretical treatments are scarce, but there is an interesting model treating the photo-refractive effect with application to $KNbO_3$ (ref. 45).

d) **Newer Models**: Some interesting models on multimode-laser dynamics were presented recently at the Quantum Electronics Laser Science Meeting (QELS) in Baltimore by many of the authors (ref. 46) who have been contributing to the frequency doubling theory. It is not clear if these new studies of antiphase dynamics are applicable to our system; however, preliminary inspection of the equations of motion indicate they are. Some of the technical paper considered basic on the chaos model are listed in ref. 47-59.

REFERENCES

1.   D. Rugar, C.J. Lin, and R. Geiss, IEEE Trans. Magn. MAG-23, 2263 (1987).
2.   E.S. Polzik and H.J. Kimble, Opt. Lett 16, 1400 (1991).
3.   L. Mandel, Opt. Commun. 42, 437 (1982).
4.   S. Kielich, R. Tanas, and R. Zawodny, J. Mod. Opt. 34, 979 (1987).
5.   K.J. McNeil, P.D. Drummond, and D.F. Walls, Opt. Commun. 28, 255 (1979).
6.   P.D. Drummond, K.J. McNeil, and D.F. Walls, Opt. Commun. 28, 255 (1979).
7.   P.D. Drummond, K.J. McNeil, and D.F. Walls, I, Opt. Acta. 27, 321 (1981); II, Opt. Acta. 28 211 (1981).
8.   G.J. Milburn and D.F. Walls, Phys. Rev. A 27, 392 (1983).
9.   L.A. Lugiato, G. Strini, and F. DeMartini, Opt. Lett. 8, 256 (1983).
10. M.J. Collett and D.F. Walls, Phys. Rev. A 32, 2887 (1985).
11. P. Gunter, Opt. Commun., 11, 285 (1974).
12. I. Biaggio, P. Kerkoc, L.S. Wu, B. Zysset, and P. Gunter, J. Opt. Soc. Am. B, 9, 507 (1992).
13. P. Gunter, P.M. Asbeck, and S.K. Kurtz, Appl. Phys. Lett., 35, 461 (1979).
14. G.J. Dixon, D.E. tanner, and C.E. Wieman, Opt. Lett. 14, 731 (1981).
15. L. Goldberg and M. Chun, Appl. Phys. Lett. 55, 218 (1989).

16. T. Baer, M.S. Keirstead, and D.F. Welch, in Digest of Conference on Lasers and Electro-Optics (Optical Society of America, Washington, DC, 1989), paper ThM5.
17. T. Baer, J. Opt. Soc. Am. B, 3, 1175 (1986).
18. R.G. Smith, IEEE J. Quantum Electron. QE-6, 215 (1970).

19. C.J. Kennedy and J.D. Barry, IEEE J. Quantum Electron. QE-**10**, 596 (1974).

20. J.D. Barry and C.J. Kennedy, J. Appl. Phys., **48**,2518 (1977).

21. V.D. Volosov, S.G. Karpenko, N.E. Kornienko, V.N. Krylov, A.A. Man'ko and V.L. Strizhevsky, "Sov. J. Quantum Electron. **6**, 500 (1975), and references therein.

22. R.R. Rice, J.R. Teague, and J.E. Jackson, J. Appl. Phys. **49**, 5750 (1978).

23. C.B. Hitz and L.M. Osterink, Appl. Phys. Lett. **18**, 378 (1971).

24. J. Falk, IEEE J. Quantum Electron. QE-**11**, 21 (1975).

25. P. Mandel and X.G. Wu, J. Opt. Soc. Am B, **3**, 940 (1986).

26. X.G. Wu and P. Mandel, J. Opt. Soc. Am B, **4**, 1870 (1987).

27. G.E. James, E.M. Harrell and Rajarshi Roy, Phys. Rev. A **41**, 2778 (1990).

28. M. Oka and S. Kubota, Opt. Lett. **13**, 805 (1988).

29. J.C. Barnmert, J. Hoffnagle, and P. Gunter, Appl. Opt. **24**, 1299 (1985).

30. A. Hemmerich, D.H. McIntyre, C. Qiommermann, and T.W. Hansch, Opt. Lett. **15**, 372 (1990).

31. W.J. Kozlovsky, W. Lenth, E.E. Latta, A. Moser, and G.L. Bona, Appl. Phys. Lett. **56**, 2291 (1990).

32. M.K. Chun, L. Goldberg, I.N. Duling III, and T.F. Carruthers, in Digest of Conference on Lasers and Electro-Optics (Optical Society of America Washington, DC, 1990), paper CWE2.

33. C.S. Adams and A.I. Ferguson, Opt. Commun. **79**, 219 (1990).

34. A. Ashkin, G.D. Boyd, and T.M. Dziedzic, IEEE J. Quantum Electron. QE-**2**, 109 (1966).

35. G.J. Dixon, Conference digest on Compact Blue-Green Lasers 1993, JWB2, p. 401.

36. T. Sasaki, Conference digest on Compact Blue-Green Lasers 1993, JWB1, p. 400.

37. M.A. Haase, J. Qiu, M.M. Depuydt, and H. Cheng, Appl. Phys. Lett. **59**, 1272 (1991).

38. T. Baer, and M.S. Keirstead, in Digest of Conference on Lasers and Electro-Optics (Optical Society of American, Washington, DC 1985), paper ThZZ1.

39. K. Tatsuno, T. Andou, S. Nakatsuka, T. Miyai, M. Takahashi, and S. Hermfrid, in Digest of Conference on Lasers and Electro-Optics (Optical Society of America, Washington, DC, 1992), paper CWQ8.

40. Y. Kitaoka, S. Ohmori, K. Yamamoto, and K.M. Kato, Conference digest on Compact Blue-Green Lasers 1993, paper JWB3, p. 403.

41. T. Sasaki, T. Kojima, A. Yokotani, O. Oguri and S. Nakai, Opt. Lett. **16**, 1665 (1991).

42. G.J. Kintz and T. Baer, IEEE J. Quantum Electron. **26**, 1457 (1990).

43. Conference digest on Compact Blue-Green Lasers 1993, JWE Session, pp. 454-467.

44. Conference digest on Compact Blue-Green Lasers 1993, CThA and CThB Sessions, pp. 468-494.

45. G. Monemezzani, M. Zgonik, and P. Gunter, J. Opt. Soc. Am. B, **10**, 171 (1993).

46. See QELS 1993 Technical Digest Series, Conference Edition QWB Session p. 130.

47. J.P. Eckmann, D. Ruelle, "Ergodic theory of chaos and strange attractors," Reviews of Modern Physics, **57**, 617 (1985).

48. E. Ott, C. Grebogi, and J.A. Yorke, in <u>Chaos</u>. ed. D.K. Campbell (American Institute of Physics, New York, 1990, pp. 153-172.

49. E. Ott, C. Grebogi, and J.A. Yorke, Phys. Rev. Lett. **64**, 1196 (1990).

50. Troy shinbrot, Edward Ott, Celso Grebogi, and James A. Yorke, "Using Chaos to Direct Trajectories to Targets," Phys., Rev. Lett. **65**, 3215 (1990).

51. J. Singer, Y-Z Wange, and Haim H. Bau, "Controlling a Chaotic System," Phys. Rev. Lett. **66**, 1123 (1991).

52. In an apparatus that was similar to one employed by H.F. Creveling, J.F. De Pazx, J.Y. Baladi, and R.J. Schoenhals, J. Fluid Mech., **67**, 65 (1991).

53. W.L. Ditto, S.N. Rauseo, and M.L. Spano, "Experimental Control of Chaos," Phys. Rev. Letts., **65**, 3211 (1990).

54. See for example, Rajarshi Roy - TuA2 and TuA3, P. Glorieux - TuA4 and TuA5 in the <u>Advanced Program for the International Second Topicla Meeting on "Nonlinear Dynamics in Optical Systems</u> - TuA, sponsored by: Air Force Office of Scientific Research, Office of Naval Research and the Optical Society of America, held at Kongresshaus Alpbach, Alpbach, Austria, 22-26 June 1992.

57. Control of Chaos - TuA, <u>Advanced Program for the International Second Topical Meeting on "Nonlinear Dynamics in Optical Systems</u>, sponsored by: Air Force Office of Scientific Research, Office of Naval Research and the Optical Society of America, hel at Kongresshaus Alpbach, Alpbach, Austria, 22-26 June 1992.

58. E. Ott, C. Grebogi, and J.A. Yorke, Phys. Rev. Lett. **64**, 119.

59. W.L. Ditto, S.N. Rauseo, and M.L. Spano, "Experimental Control of Chaos," Phys. Rev. Letts., **65**, 3211 (1990).

APPENDIX B

LASER IMAGING RADAR SYSTEM (LIRS)

This radar transmitter will use blue-green wavelength for the
penetration in ocean water

Reprinted from

Laser Radar VII:
Advanced Technology
for Applications

P

Volume 1633

Diode-laser radar for low-cost weapon guidance

Robert L. Gustavson

Schwartz Electro-Optics, Inc.
3404 North Orange Blossom Trail
Orlando, Fl 32804

Thomas E. Davis

WL/MNGS
Eglin AFB, FL 32542-5434

ABSTRACT

Since 1986, the USAF Wright Laboratories, at Eglin Air Force Base has conducted a series of related test programs and technology development activities with the purpose of determining the feasibility of using diode-laser radar systems as sensors for autonomous targeting guided weapons. Schwartz Electro-Optics, working under a USAF contract to develop a diode-laser radar for submunition applications, has developed a real-time (30 Hz frame rate) imaging diode-laser radar system which employs a proprietary algorithm for target recognition and classification. In captive flight testing using a remotely piloted vehicle (RPV), the system has been used to detect, classify, and determine aim-points of targets (tanks, trucks) in a high-clutter environment; false-color range and gray-scale reflectance imagery were displayed in real time. The testing yielded excellent target acquisition performance. The 42,000 frames of range and reflectance data which were obtained during the testing are being used for further development of the target recognition and classification (TRAC) algorithm. This paper reviews the imaging diode-laser radar development and the captive flight test program.

1. INTRODUCTION

In late 1985, the USAF Air Force Armament Test Laboratory at Eglin AFB, FL began a program whose purpose was to examine the feasibility of using direct illumination diode-laser radar systems for autonomous targeting anti-armor submunition applications. The appeal of diode-laser radar is its ranging and three-dimensional profiling capabilities which have the potential to make it a very effective submunition sensor. The capability to measure range improves kill probability because warheads may be fired at optimum standoff distance. Three-dimensional profiling facilitates improved target recognition, thereby reducing susceptibility to false alarms. Profiling also permits determination of optimum aim-point on the target, which improves kill probability. Also appealing is its potential for very low cost (compared to other sensor options), which is of extreme importance for autonomous guidance. A key component of the program is a contract awarded to Schwartz Electro-Optics, Inc. (SEO) of Orlando, FL. Under the contract, SEO recently (September, 1991) conducted a series of captive flight tests at Eglin AFB. This paper reviews the highlights of the diode laser radar development program, including results from the September 1991 captive flight tests and future program plans.

The initial phase of the program, begun in December 1985, consisted of fabricating a single-element diode-laser range finder and scanning system and integrating it with the image data display and recording hardware necessary to conduct an armored target/vehicle image data collection program at the Eglin AFB range C52 300 foot tower. This program phase culminated in a successful data collection activity in 1988.

Following the initial single-element range finder phase of the program, a more ambitious task based upon a scanning array implementation was begun. The scanning array ladar program also included a target

detection and classification algorithm development task, and, as reported elsewhere[1,2], it concluded with a successful tower test program in 1989. The tower test program is described in Section 2 below.

Following the tower test phase of the program, a captive flight test phase, employing the scanning array ladar system in a remotely piloted vehicle (RPV), was begun in 1990. The captive flight test phase, which is nearing completion, is described in Section 3 below.

In the process of announcing the flight test program results to potential user organizations at Eglin AFB, an interest in the RPV/ladar system by the Air Base Operability System Program Office became apparent. The potential application is the use of the system for remote bomb-damage assessment of runways. As a consequence of discussions arising from that interest, a flight test program extension to conduct a preliminary feasibility assessment is currently being negotiated, as discussed in Section 4 below.

2. TOWER TEST PROGRAM

2.1. Single-channel range finder

A block diagram of the single-channel range finder is presented in Figure 2.1-1. The range finder is comprised of six subsystems: the laser transmitter, the optical receiver, the range counter, the reflectance measurement unit, the scanner, and the computer.

The single-channel range finder is a pulse time-of-flight type, which is designed to measure range to non-cooperative (10% lambertian) targets at a maximum range of approximately 200 meters with a range resolution of 10 cm and an angular resolution is 10 mr.
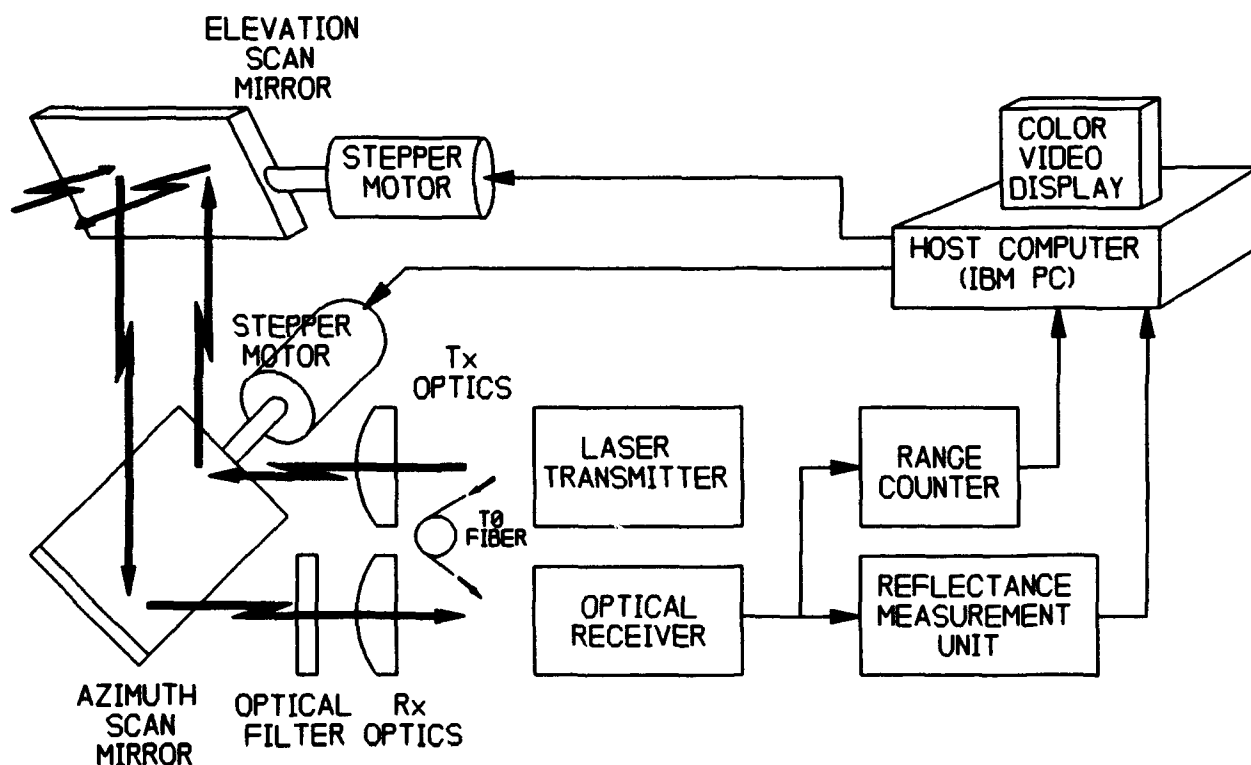
Fig. 2.1-1 Single-channel laser rangefinder block diagram

2.1.1. Laser transmitter

The transmitter consists of a diode laser and a pulser. The GaAlAs metal organic chemical vapor deposition (MOCVD) diode laser emits 6 ns (FWHM) light pulses at a wavelength 850 nm and at a repetition rate of 9 kHz. The diode laser is driven with 30 A current pulses, which are produced by the avalanche effect in a common small-signal transistor.

Unlike most lasers, the semiconductor diode laser emits radiation into a rather large solid angle. Consequently, it is necessary to employ an optical system to collect the radiation and to shape it into a narrow beam. In order to collect as much of the laser energy as possible, it is necessary to use an optical system with a large collection cone. This implies a fast optical system, or a low "F" number. The single-channel laser transmitter has a 2 inch clear aperture F1.4 lens, which collects approximately 50 percent of the laser's 60 Watt pulse.

2.1.2. Optical receiver

The optical receiver consists of an avalanche photodiode (APD) and a transimpedance amplifier. The APD acts as a current source together with the integrated circuit (IC) transimpedance amplifier, which converts the APD's current pulses to voltage pulses.

Background irradiance is the main source of noise in a wide-field-of-view receiver which has an APD detector. The background irradiance is reduced by an optical interference filter having a bandwidth of 40 nm (FWHM) at 850 nm. The optical filter passes the broad temperature-dependent spectral output of the diode laser without the need to cool the diode laser.

2.1.3. Range counter

The range counter consists of a constant-fraction threshold detector (CFTD) and a time-to-amplitude converter (TAC). The CFTD produces accurate, logic-level, start, and stop pulses for the TAC. The TAC generates a dc voltage which is proportion to the time between the start and stop pulses which is related to the range through $\Delta t = 2R/C$, where C is the speed of light.

The timing start pulse is produced optically by detecting the transmitted light pulse, which reduces timing errors caused by time delay changes within the transmitter. A short optical fiber placed between the diode laser's output beam and the optical receiver's FOV is used to generate the start pulse.

The CFTD is an adaptive thresholding system, which determines pulse arrival time in a way that is independent of pulse amplitude. Variation of target reflectance and the distance between the receiver and the target causes amplitude variations in the received return pulses. In the stop pulse generation the CFTD must be able to handle a wide dynamic range.

In the TAC, a capacitor is discharged by a constant-current source from a reference voltage. The amount of discharge is proportional to the time difference between the start and stop pulses. The capacitor voltage is acquired by a sample-and-hold amplifier and then converted to digital format for readout by the computer. The TAC is a relatively simple circuit that provides very good range resolution for shorter range (< 500 M) applications.

2.1.4. Reflectance measurement unit

The output from the optical receiver is a train of narrow pulses whose amplitudes contain information about the reflectivity of the target. Each range interrogation produces a pair of pulses out of the optical receiver, where the first pulse (T_o) is the optical "start" pulse for the range counter, and the second pulse, the target return, is the "stop" pulse for the range counter.

Because of the narrow pulses involved (6ns FWHM), the signal processing system must employ very-high-speed analog circuits. Since the return pulse is preceded by the laser T_0 pulse, the first element in the signal-processing system must be a high-speed gate which stops the T_0 pulse but allows the return pulse to enter. Once the target return pulse enters, its peak value must be held for a sufficient time to permit analog-to-digital conversion. The output voltage of the peak detector must be quickly resetable to accommodate the high pulse repetition rate (9 kHz). Accuracy of peak amplitude detector must be maintained despite varying pulse amplitude (dynamic range > 40 dB).

2.1.5. Scanner

The scanner consists of two front-surface silver flat mirrors driven by computer controlled stepper motors as shown in Figure 2.1-1. The mirrors are stepped in a raster format to form a 4 by 8 degree field of regard.

2.1.6. Computer

An IBM portable computer (PC) with integral digital signal processor (DSP) card is used to control the scanning mirrors, read range and reflectivity data from the range finder, display a false-color range image, and pass the data to the DSP. The DSP, a Texas instruments 320C25, preforms a target classification algorithm.

2.2. Profile target algorithm

The profile target algorithm was originally developed for use with a single-channel laser range finder and was designed to classify a target using only a single scan across the target. The testing scenario included only M-48 tanks and M-35 trucks in ideal conditions, with minimal clutter and no counter-measures. The profile target algorithm is comprised of three modules -- the preprocessor, profile encoder, and a rule-based classifier as shown in Fig. 2.2-1. The modules were designed to pass the data through in pipeline fashion so that an embedded system which uses parallel processing could be accommodated if necessary.
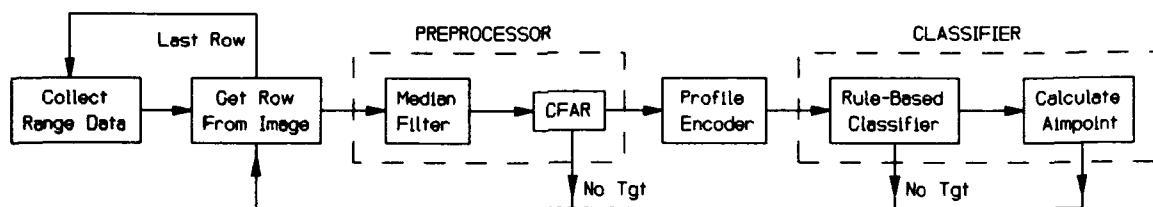
Fig. 2.2-1 Profile target algorithm

2.2.1. Preprocessor

Raw range data are initially sent to the preprocessor for filtering. A five-sample median filter is passed over the data, with the center sample being replaced with the median value. The filter is then shifted by one sample until all of the data have been filtered. The filtered range data are then converted to elevation data by first estimating a ground zero reference point. Ground zero is estimated by calculating the median of random samples across the scan line. The range data are then normalized for any angular distortions which may be caused by the scanning mechanism, and stored as elevation relative to ground zero.

The elevation data are processed by a Constant False Alarm Rate (CFAR) algorithm. The CFAR algorithm provides initial detection of objects by calculating simple statistics, such as the mean and variance, of the

range elevation data for three data gates -- a lead gate, a lag gate, and a target gate. The elevation data samples shift through these gates, entering the lead gate first and exiting through the lag gate. The size of each gate is dynamic and must be wide enough to contain all of the samples belonging to a desired target. The CFAR algorithm waits until a target is centered in the target gate before passing the data to the profile encoder. The CFAR tests which are preformed, assume that the data in the lead and lag gates are representative of the terrain. If there is significant variation in the terrain, the target may not be detected.

The CFAR algorithm conducts four tests to determine if a target is present. The first test examines the average height, or elevation, of the samples in the target gate to insure that it is below some dynamic threshold. The maximum threshold is set based upon the heights of targets to be detected. If data in the lead and lag gates indicate that the terrain may be "hilly", the threshold is adjusted to allow for a target which may be sitting on a hill. The second CFAR test compares the average height of samples in the target gate with a minimum threshold to confirm it is sufficiently high to be a valid target. If the first two tests generate passing results, each sample in the target gate must be tested to see if it falls within the minimum and maximum height thresholds. There must be enough samples in the target gate that satisfy this requirement for a valid target to be present. The final test checks the variance of the samples in the target gate against two constants related to the type of terrain that is expected.

2.2.2 Profile encoder

The profile encoder operates on the data in the target gate if all CFAR tests yield positive results. The profile encoder creates an array of relative elevation changes between two adjacent samples. The array contains positive and negative values if the elevation is increasing or decreasing respectively, or zero values if the elevation remains constant over a series of samples, as shown in Fig. 2.2.2-1. The profile encoder generates a profile structure table which contains all of the trends found in the data. The encoder recognizes five features, a plateau, a rising or falling edge, and a positive or negative peak. A plateau must contain at least five consecutive samples at the same elevation. Any plateau with less than five samples is assimilated into one of the other four trends. A positive or negative peak is defined by a rising or falling edge which does not end at a plateau. The number of samples and the elevation of each plateau are also contained in the profile structure table.

2.2.3 Rule-based classifier

The rule-based classifier makes the final decision as to whether the object is a valid target. The classifier uses a feature set which includes the total number of plateaus, the maximum elevation of a plateau, the relative sizes of the plateaus, and the orientation of the plateaus to make a decision. Actual data from an M-48 tank and an M-35 truck were used to extract the feature set. The feature set was tested against a training set of images to validate its effectiveness in classifying targets under ideal conditions. An aim-point was generated by calculating the midpoint of the highest and longest plateau. This produced an aim-point that was on the turret of the tank and on the canopy area of the truck.

2.3. Tower test results

Figures 2.3-1 and 2.3-2 demonstrates the performance achieved with the single-channel diode laser range finder. As noted, the tower test consisted of the single-element range finder being scanned in azimuth and elevation. For each pixel (azimuth and elevation angle location) measured range and reflectance are stored. From the stored data a 3-D computer calculated false-color range image and gray-scale reflectance image was made. One has no problem telling that the measured data displayed in the two figures is that of a tank.

The profile target algorithm generated acceptable results for classifying targets using only a single scan line. However, rejecting clutter proved to be a more difficult task. Measured clutter data produced target-like profiles. Further testing was done by processing a combination of multiple scan lines and combining the

```
FILE: TRUCK51.IMG        MIN:   0    MAX:   9    LINE #:  26    COLUMNS:  93

                              ****************************
                                                          ********
                                                        **
                                                          *******
                    *

 *********************                                            *
                    *                                            *
**********************                                           ****************
---------------------------------------------------------------------------------

00000000000000000000000000+++0000000000000000000000000000000-00000000-0-0000000---000000000000000

PPPPPPPPPPPPPPPPPPPPPPPPPP+++PPPPPPPPPPPPPPPPPPPPPPPPPPPPPPPP-PPPPPPPP---PPPPPPP---PPPPPPPPPPPPPPPP

11111111111111111111111112221111111111111111111111111111113111111111333111111113331111111111111111
```

PROFILE STRUCTURE

```
------------------
Plateau              +++ SIZE: 25 *** ELEVATION:  0
Rising edge
Plateau              +++ SIZE: 30 *** ELEVATION:  9
Falling edge
Plateau              +++ SIZE:  9 *** ELEVATION:  8
Falling edge
Plateau              +++ SIZE:  8 *** ELEVATION:  5
Falling edge
Plateau              +++ SIZE: 16 *** ELEVATION:  0
```

Fig. 2.2.2-1   Profile plot of an M35 truck

results from those scan lines to produce a single result. This greatly increased the probability of detection while significantly reducing the probability of false alarms. The results were sufficiently good enough to warrant the development of a multi-channel sensor along with an enhanced target algorithm to process he data.

Fig. 2.3-1 False-color range image of an M48 tank   Fig. 2.3-2 Gray-scale reflectance image of an M48 tank

3. FLIGHT TEST PROGRAM

3.1. 24-channel real-time imaging LADAR

Design goals for the flight test program included the following:

1) Maximum range performance of 500 M.
2) 30 Hz frame rate.
3) 4° x 10° field-of-regard.
4) Packaging for testing from a remotely pilot vehicle (RPV).
5) Real-time display of false-color range and gray-scale reflectance imagery.
6) Real-time target classification and aimpoint determination.

The block diagram of the 24-channel real-time imaging LADAR is presented in Figure 3.1-1. This real-time imaging Ladar uses a 24 element laser array and co-aligned 24 element APD array, which is scanned by a rotating four-sided mirror. The 24-channel system design is based on the same circuit topology described previously in section 2.
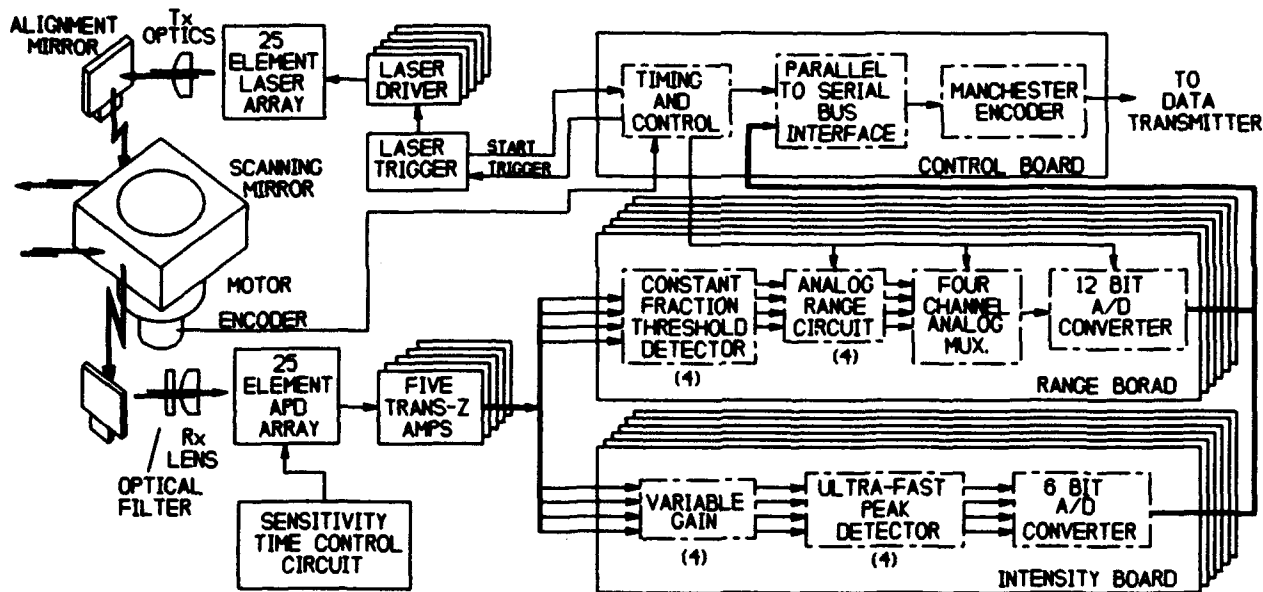
Fig. 3.1-1 24-channel real-time imaging LADAR block diagram

3.1.1. Laser transmitter

The transmitter is a 24 element MOCVD diode laser array. Each of the lasers in the linear array produces 120 W at 850 nm. Separated by 0.015 of an inch, each diode laser element is 0.010 inches by 0.012 inches. A 6.4 cm clear aperture F2 lens produces twenty-four 3 mr beams.

3.1.2. Optical receiver

The receiver consists a 24 element APD array (RCA C ^985) and 24 transimpedance amplifiers. The geometry of the APD array is similar to that of the laser array.

3.1.3. Range counters and reflectance measurement

The 24 range counters and reflectance measure measurement circuits are almost identical to those described in section 2. To reduce space and power consumption quad components and device multiplexing was used were possible. As shown in Figure 3.1-1 there are six range counter pc-boards and six reflectance measurement boards each with four channels.

3.1.4 Scanner

The scanning system consist of a mirror cube, a constant velocity motor and an optical shaft encoder, as shown in Figure 3.1-1. The four-sided mirror spins at 7.5 rev/sec (450 RPM) to provides the 30 Hz frame rate. The encoder provides position dependent control for the range finder timing and control circuit.

3.1.5 RPV

The RPV used for the flight testing is a fiberglass/foam composite structure custom-built by Aero Composites Inc. The twin-boom pusher prop aircraft measures 9.6 feet in length with a 14 foot wingspan. The RPV gross weight is 200 pounds, and it is capable of carrying a 65 pound payload. Fully loaded, the RPV can cruise at 80 MPH for approximately two hours on two gallons of gasoline.

3.1.6 Telemetry

There are five microwave telemetry links between the RPV and the ground station -- one data and two video links from the RPV and two control links to the RPV. The data link transfers the manchester-encoded range and intensity information to the ground station at a continuous 820 kHz rate. The video links transfer the forward looking camera video, used for target alignment, and the down looking camera video which is boresighted with the range finder. The primary and back-up control links are completely independent links for aircraft control. The controls include an autopilot, heading hold and altitude hold electronics.

3.1.7 Ground station

The function of the ground station is to acquire, process and store the range finder data and video as well as RPV flight control. The video assembly consists of two microwave receivers, video recorders and monitors to acquire and store the look-down and look-ahead videos. The look-down video can also be mixed with the computer range/intensity image onto one screen. The ground station computer is a 33 MHz 386 PC AT with an Intel 860 processor card for handling real-time image processing. The real-time processing includes target classification and aim-point determination. The computer system also contains a 650 MB rewriteable optical disk for storing the range finder data. At 30 frames per second, one minute of data collection require 9 MB. The flight control system consists of a primary and a back-up radio control unit, each interfaced to a microwave transmitter. Each system is an independent nine-channel PWM (Pulse-Width Modulated)unit with battery back-up for both transmitters.

3.2. 3-D Target algorithm

The 3-D target algorithm was designed to be more robust than the profile target algorithm, providing better target classification within an abundance of clutter and minimal counter-measures. An entire frame of 24x60 samples is processed in real-time at a frame rate of 30 Hz. The 3-D target algorithm is divided into three modules -- the preprocessor, recognizer, and classifier. The main functions of the modules are shown in Fig 3.2-1.

3.2.1. Preprocessor

The preprocessor accepts a frame of raw range data and outputs a filtered elevation image. It does not try
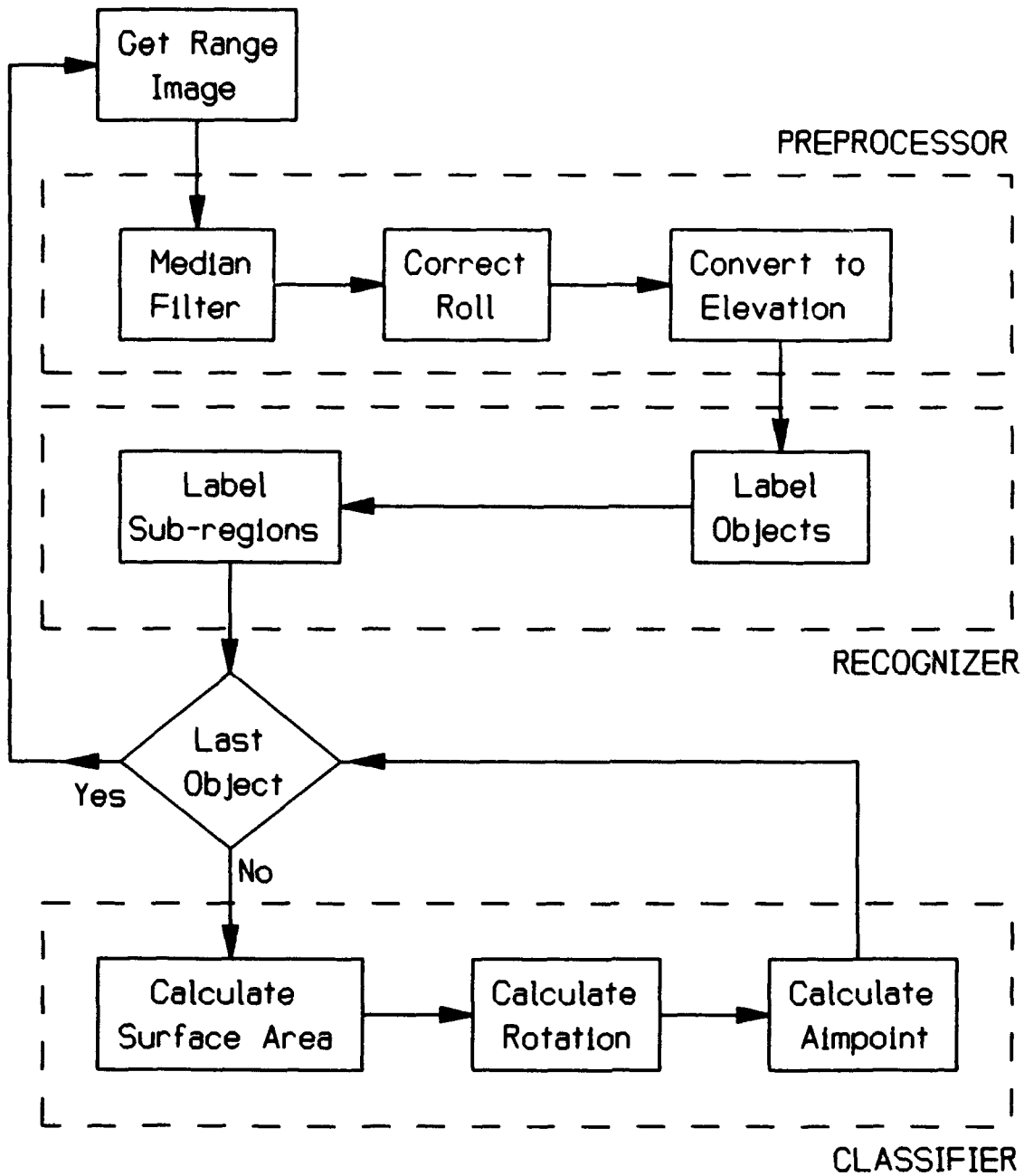
g. 3.2-1 3-D target algorithm

to do any initial target detection or rejection. The range data are filtered using a 1-D three-sample median filter which is run across each row and then down each column. A 1-D median filter was chosen over a 2-D 3x3 median filter because the 1-D filter provided acceptable results and required less time to filter an image.

After the range data have been filtered, the preprocessor is responsible for estimating the amount of roll present in the image. During flight, it is possible that the sensor may not be completely level while collecting data. Currently, there are no hardware devices on the sensor to provide the target algorithm with the correct altitude, roll, and pitch of the sensor. The algorithm must estimate these values based upon the range data. Any skewing of the data will affect the creation of the elevation image. The roll of the sensor is estimated by calculating a first-order least-squares fit on selected rows of the image. An error function is generated, all samples with excessive error are eliminated and a second fit is calculated. The slope of this line is used to determine the roll of the sensor; then all range samples are adjusted accordingly.

A ground zero plane is estimated by calculating the median of various samples throughout the range image. The range data are normalized for all angular offsets, then stored as elevation data relative to the ground zero plane.

3.2.2. Recognizer

The recognizer scans through the elevation image and identifies and labels all objects in the image. The recognizer sets a minimum elevation threshold of 4 feet and a maximum threshold of 12 feet. Any samples that do not fall within these thresholds are removed from the image. The remaining samples are assigned labels. Samples that are adjacent to one another are assigned identical labels. There will be one label for each object in the image. The classifier uses this labeled image as a mask to extract each object from the image for independent classification.

To provide better target classification, the recognizer also identifies sub-regions within each object. The samples belonging to sub-regions must have an elevation of at least 8 feet. By labeling the sub-regions of each object, information is provided about the internal structure of each object. For the selected target set, the sub-regions should include the tank turret and the cab and/or canopy area of a truck.

3.2.3. Classifier

Using the labeled image mask which was generated by the recognizer, the classifier extracts one object at a time for target classification. The first feature that is calculated is the surface area of the object. This is the primary discriminator for rejecting objects early in the classification process. Additional features are calculated for objects having acceptable surface areas.

The structure of an object is validated by examining the ratio of the surface area of the sub-regions to the total surface area of the object. For example, for an object to be classified as a tank, it must possess a turret, which is a sub-region comprising a certain percentage of the surface area of a tank.

To eliminate objects having surface areas similar to that of the selected targets, the ratio of the perimeter of the object to the total surface area is calculated. All of the targets in the target set are rectangular in shape, and thus produce predictable ratios. This feature rejects objects having irregular shapes.

The object is then rotated to a major axis so that three rotation-based features can be calculated. Two of these features simply verify the size of the object by calculating the length-to-width ratio and the average width of the object. The third feature calculates a ratio between the number of samples in the object and the number of samples which fill a rectangular region that totally encompasses the object. Irregular-shaped objects produce a lower ratio because a larger region is needed to encompass them.

Once a target has been classified, the coordinates for an aim-point are calculated. The classifier selects the

centroid of the sub-region of the target as the aim-point. This places the aim-point on the tank turret or on the cab or canopy area of the truck. These aim-points were arbitrarily selected and may be changed to other areas of interest on the targets.

3.3. Test results

Figure 3.3-1 demonstrates the performance achieved with the 24-channel diode laser radar. Included in this real-time display is a 3-D color range/elevation image and a gray-scale reflectivity image. The color bar in the lower right can be used to determine target/object height in feet. Also included in the display are target aimpoint location, target classification and RPV altitude in feet.

During the first Captive Flight Test (CFT) of the sensor, the 3-D target algorithm produced very good results with a high probability of detection and an extremely low probability of false alarm. Over 43,000 frames of data were collected and processed in real-time. Enhancements have been made to the target algorithm to increase the probability of detection even further using the data from the CFT.
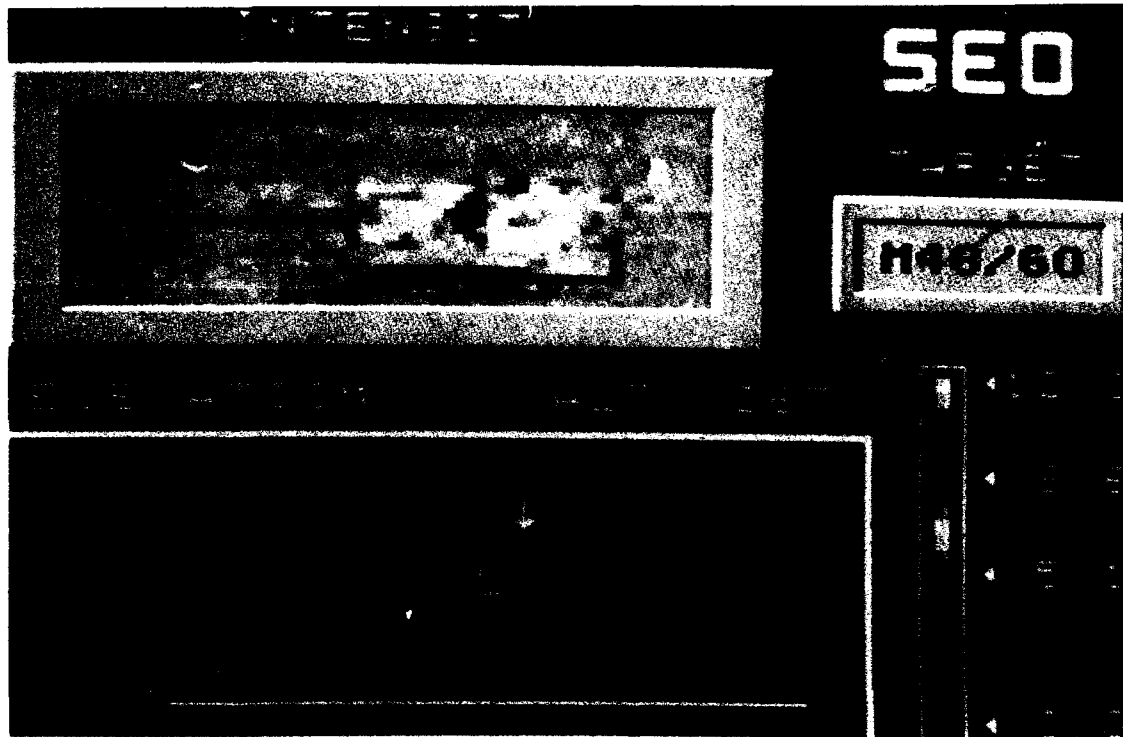
Fig. 3.3-1 24-channel laser radar real-time false-color range and gray-scale reflectance display

4. CONCLUSIONS

Results collected in the flight test phase of the diode laser radar development program provide a promising foundation for a very low cost short-range weapon guidance sensor appropriate for applications such as smart submunition guidance. However, a fundamental limitation of the current version of the system is the beam divergence exiting from the transmitter diodes, and consequently the optics necessary to collimate the transmitted beam to useable divergence. The diode beam divergence is on the order of 40 degrees, and the

current system collimates that beam to 3 mr using an optics system with approximately 6" focal length and 2.5" clear aperture. The optics size/beam divergence tradeoff significantly complicates the problem of packaging the sensor for the extremely demanding package-size requirements of submunition guidance applications, and a key component of the future plans for the development program centers around efforts to alleviate this complication.

As noted in the introduction, during the captive flight test phase of this program, a runway bomb damage assessment role appeared as a possible application for this technology. The operational requirements of this mission appear to be well suited to the RPV/ladar combination and a contract modification is currently being negotiated to include a preliminary investigation (via captive flight testing) of this application.

5. ACKNOWLEDGEMENTS

6. REFERENCES

1. D. Crane and P. Verges, "Compact Solid-State Ladar" Proceedings of the 1990 National IRIS Meeting, August 1990.
2. D. Crane and P. Verges. "Compact Solid-State Ladar Update" Proceedings of the 1991 National IRIS Meeting, June 1991.

APPENDIX C:

FEEDBACK USING EXTERNAL RESONATOR

"OPTICAL RESONATOR WITH AN EXTERNAL SOURCE: EXCITATION OF THE HERMITE-GAUSSIAN MODES"

Optical resonator with an external source: excitation of the Hermite-Gaussian modes

M. R. Sayeh, H. R. Bilger, and T. Habib

The amplitudes of excited Hermite-Gaussian modes in an astigmatic resonator due to an injected astigmatic Gaussian mode are calculated. Various types of misadjustment are considered: offset ϵ; tilt α; mismatch o. For small misadjustments the amplitudes are fast-converging series in the mismatch parameter o and in the misalignment parameter ξ. For mismatch, only even-indexed Hermite-Gaussians appear. The theory is applied to an experimental result involving a 3.15-m square ring interferometer. Formulas for power matching are derived, and control loops to eliminate all but the Gaussian mode are proposed.

I. Introduction

The ideal situation of a perfectly coupled system of a source with a passive resonator via a matching and aligning circuit is given in Fig. 1. The adjustment box has two purposes:

(a) It aligns the optical axis of the injecting laser beam with the optical axis of the resonator modes.

(b) It matches the spatial distribution of the injected beam mode with the distribution of the corresponding resonator mode. (Frequency matching [tuning] is not discussed in this paper.)

Figure 1 depicts a ring resonator as a case of an astigmatic resonator. However, we will limit the discussion to resonators where two orthogonal symmetry axes exist, one in the plane of the ring (x axis) and another perpendicular to this plane (y axis).

Unlike a self-aligning optical oscillator (laser), such a resonator has its own eigenmodes independent of the injected beam so that imperfect spatial coupling necessarily excites unwanted modes for any degree of misadjustment, be it misalignment or mismatch: unlike the self-excited laser, there is no threshold either for higher-order modes.

The purpose of adjustment is thus to effect a perfect spatial overlay mode by mode of a laser beam with the corresponding resonator modes.

This analysis attempts to quantify the effects of misadjustment. Of the many types of mode realizable, only Hermite-Gaussians are used because they are the most commonly occurring; they can be natural-

ly extended to systems with two orthogonal planes of symmetry, as is the case in ring resonators; misadjustment can be separately discussed in each plane; conversely, the simpler case of a linear resonator can be obtained in a straightforward manner.[1]

The formalism of astigmatic Hermite-Gaussian modes (HGs) is developed in Sec. II. The expansion of a beam in the resonator's eigenmodes is formalized in Sec. III. We inject a misadjusted Gaussian beam (Sec. IV) and expand it in the resonator's modes (Sec. V). The resulting general equation is then used to predict power matching, i.e., the degree to which power is transferred from the beam to the Gaussian of the resonator (Sec. VI). Formulas for the HGs are then developed and specialized to misalignment and mismatch in Sec. VII. Finally, the analysis is applied to empirical data obtained on a square ring where misadjustment parameters are quantitatively assessed from a measured spectrum of HGs (a scan) (Sec. VIII). A summary of the results and consequences is drawn in Sec. IX.

II. Astigmatic Hermite-Gaussian Modes

HGs solve the Fresnel-Kirchhoff diffraction integral as well as the paraxial wave equation.[2] For purposes of this analysis we will discuss the electric field of a HG polarized in the $\hat{x}$ direction ($\hat{x}$ is a dimensionless unit vector), propagating in the positive z direction (the optical axis), in vacuum:

$$E_{mnq}(x,y,z,t) = \sqrt{(2\eta P_{mn})}U_{mn}(x,y)\exp(-jkz + j\omega t)\hat{x}, \quad (1)$$

where η = vacuum impedance = $(\mu_0/\epsilon_0)^{1/2}$, P_{mn} = beam power, k = wave number, ω = angular frequency, with

$$U_{mn}(x,y) = U_m(x)U_n(y) = \{[\sqrt{2}/(\sqrt{\pi}2^m m!w_x)]^{1/2}H_m(\sqrt{2}x/w_x)\}$$
$$\times \exp[-j(k/2q_x)x^2 + j(m + 1/2)\phi_x]\}$$
$$\times \{[\sqrt{2}/(\sqrt{\pi}2^n n!w_y)]^{1/2}H_n(\sqrt{2}y/w_y)$$
$$\times \exp[-j(k/2q_y)y^2 + j(n + 1/2)\phi_y]\}. \quad (2)$$
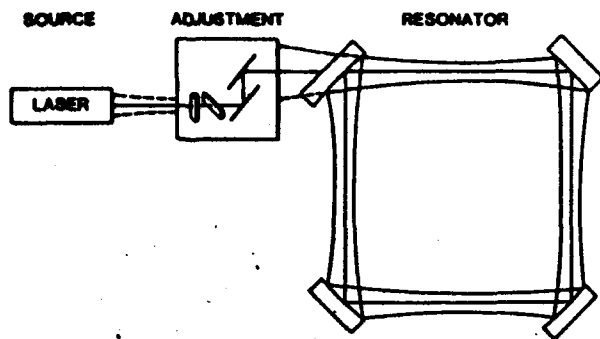
Fig. 1. Laser source coupled into a resonator via an adjustment circuit. The function of the latter is to align and match the source to the (astigmatic) resonator.

Fig. 2. Misaligned system: The laser's optical axis z' is offset by ϵ and tilted by α against the resonator's optical axis z. In this figure the waists of laser and resonator are at the same z and equal in size.

This is the astigmatic formulation of the lateral field distribution, where w_x, w_y are the spot sizes in the x and y directions, respectively (the spots are generally elliptical), H_m and H_n are Hermite polynomials of degree m and n, respectively, q_x and q_y are the complex curvature parameters, and ϕ_x and ϕ_y are phases.

The Hermite-Gaussian function $U_{mn}(x,y)$ is thus completely separated into a product of two functions, each depending only on one lateral variable. Since all operations below preserve this independence, we will treat one variable only: $\mu = m$ or n, $\nu = x$ or y. We have then $H_\mu(\nu)$, with $H_0(\nu) = 1$, $H_1(\nu) = 2\nu$, $H_2(\nu) = 4\nu^2 - 2$, etc., and

$$q_\nu^{-1} = R_\nu^{-1} - j2/kw_\nu^2 \quad (R_\nu = \text{curvature radius}). \quad (3)$$

The fields E_{mnq} are normalized so that

$$1/2 \int_{-\infty}^{+\infty} \int_{-\infty}^{+\infty} (E_{mnq}^* E_{mnq}/\eta) dx dy = P_{mn}, \quad (4)$$

i.e., P_{mn} is the power of the mnq mode. The HG functions are normalized so that

$$\int_{-\infty}^{+\infty} |U_\mu(\nu)|^2 d\nu = 1.$$

Useful approximations for phase ϕ_ν, spot size w_ν, and curvature radius R_ν:

All modes have the same dependence of z. For the phase,

$$\phi_\nu(z) = \tan^{-1}[(z - z_{0\nu})/z_{R\nu}], \quad (5)$$

where the argument of $\tan^{-1}$ is the distance from the waist site $z_{0\nu}$ in terms of the Rayleigh range $z_{R\nu}$. In a system which is not far from adjustment, we can assume that all waists are well within the Rayleigh ranges of each other, and we may approximate $\phi_\nu \simeq 0$. For the curvature radii, we have

$$R_\nu(z) = (z - z_{0\nu})[1 + z_{R\nu}^2/(z - z_{0\nu})^2]. \quad (6)$$

Again we may occasionally put $R_\nu \to \infty$ close to the waist sites, in which case $q_\nu(z)$ becomes purely imaginary, $q_\nu \to jkw_{0\nu}^2/2$. Finally the spot sizes are

$$w_\nu^2(z) = w_{0\nu}^2[1 + (z - z_{0\nu})^2/z_{R\nu}^2] \quad (7)$$

and may be approximated by their respective waist sizes $w_{0\nu}$.

III. Expansion of an Injected Beam into the Resonator's Eigenmodes

The functions U_{mn} form an orthogonal and complete set.[3] We, therefore, expand the x component of the field E_L of an injected beam in terms of this set, i.e.,

$$E_L = \sum_{m=0}^{\infty} \sum_{n=0}^{\infty} A_{mn} E_{mnq} \quad (E_L = x \text{ component of injected field}) \quad (8)$$

with dimensionless but generally complex expansion coefficients A_{mn}. The fields E_{mnq} are given by Eq. (1), where $P_{mn} = P_L$ (power of the injecting beam). We have

$$\sum_{m=0}^{\infty} \sum_{n=0}^{\infty} |A_{mn}|^2 = \sum_{m=0}^{\infty} |A_m|^2 \sum_{n=0}^{\infty} |A_n|^2 = 1, \quad (9)$$

$$A_\mu = \int_{-\infty}^{+\infty} U_\mu^*(\nu) U_L(\nu) d\nu, \quad (10)$$

where $U_\mu^*(\nu)$ is the conjugate-complex of the μth eigenmode, and $U_L(\nu)$ is the HG function of the injected E field.

IV. Injection with Misadjusted Gaussian Beam

In the following we use an injected astigmatic Gaussian beam ($m = n = 0$) with spot sizes w_{Lx} and w_{Ly}. Its optical axis shall be parallel-shifted against the resonator's z axis by ϵ_x and ϵ_y in the x and y directions, respectively. It shall also be tilted by angles α_x and α_y off the resonator's z axis (see Fig. 2). Finally we allow the waist sites of injected beam and resonator modes to be different as well as the waist sizes (see Fig. 3).

The integrals [Eq. (10)] are evaluated in the coordinate system of the resonator: $x =$ in-plane coordinate of resonator; $y =$ perpendicular to plane; $z =$ optical axis of ring, forming a right-handed coordinate system, origin at waist location.

In the tilted and offset coordinate system $x'y'z'$ of the injected beam, the field distribution is

$$\mathbf{E}_L(x',y',z',t) = \sqrt{(2\eta P_L)}(2/\pi w_{Lx} w_{Ly})^{1/2}$$
$$\times \exp[-j(k/2)(x^2/q_{Lx} + y^2/q_{Ly})]$$
$$\times \exp(-jkz' + j\omega t)\hat{x}'. \quad (11)$$

This results from Eqs. (1) and (2) with $\mu = 0$, $\phi_\nu = 0$.

Expressing the primed coordinates in the unprimed coordinates of the resonator system, we have

$$x' = (x - \epsilon_x)\cos\alpha_x \qquad\qquad -z\sin\alpha_x \qquad \simeq x - \alpha_x z - \epsilon_x,$$

$$y' = (x - \epsilon_x)\sin\alpha_z\sin\alpha_y + (y - \epsilon_y)\cos\alpha_y - z\cos\alpha_z\sin\alpha_y \simeq y - \alpha_y z - \epsilon_y, \qquad (12)$$

$$z' = (x - \epsilon_x)\sin\alpha_z\cos\alpha_y + (y - \epsilon_y)\sin\alpha_y + z\cos\alpha_z\cos\alpha_y \simeq z + \alpha_x x + \alpha_y y,$$

retaining only terms of first order in the misalignment parameters ϵ_x, ϵ_y, α_x, α_y.

The pivot point is assumed to be at $z = 0$. For small deviations from $z = 0$, the errors are of second order in the parameters.

Furthermore, $\tilde{x}' = \tilde{x}\cos\alpha_x - \tilde{z}\sin\alpha_x \simeq \tilde{x}$ is set. The $\tilde{z}$ component is eliminated because it is orthogonal to $\tilde{x}$.

The field of the injected beam is, therefore, approximately $\mathbf{E}_L(x,y,z,t) = (2\eta P_L)^{1/2}U_L(x,y)\exp(-jkz + j\omega t)\tilde{x}$, with

$$U_L(\nu) = [\sqrt{2}/(\sqrt{\pi}w_{L\nu})]^{1/2}$$
$$\times \exp[-j(k/2q_{L\nu})[\nu^2 - 2(\epsilon_\nu - q_{L\nu}\alpha_\nu)\nu + \epsilon_\nu^2]] \qquad (13)$$

V. Expansion of Injected Field in the Resonator Eigenmodes

Equations (2), (10), and (13) are used in a physical situation where the waist sites in the two planes are well within the respective Rayleigh ranges of each other, so that we can put $\phi_x = \phi_y \simeq 0$ and also $jkw_\nu^2/2 \simeq q_\nu \simeq q_\nu^*$. Equation (13) yields

$$A_\mu = \int_{-\infty}^{+\infty} U_\mu{}^*(\nu)U_L(\nu)d\nu.$$

It is convenient to introduce a misalignment parameter ξ and a mismatch parameter o, namely,

$$\xi_\nu = (\epsilon_\nu - q_{L\nu}\alpha_\nu)w_\nu \qquad o_\nu = [(q_\nu{}^* + q_{L\nu})/(q_\nu{}^* - q_{L\nu})]^{1/2}, \quad (14)$$

where the offset is measured in units of the spot size, the tilt in units of beam divergence, and the mismatch in terms of the ratio of the complex curvatures. Note that for perfect adjustment, $\xi_\nu = o_\nu = 0$. For coinciding waist sites, the mismatch parameter o can be written as $o_\nu = [(w_\nu^2/w_{L\nu}^2 - 1)/(w_\nu^2/w_{L\nu}^2 + 1)]^{1/2}$, i.e., in terms of the waist sizes directly. The amplitudes are then evaluated from the integral (10)[4]. The result can be written in the form

$$A_\mu = W_\nu \times \Xi_\nu \times M_{\mu\nu}$$

with

$$W_\nu = [(w_\nu/w_{L\nu})2q_{L\nu}/(q_{L\nu} + q_\nu)]^{1/2} = (1 - o_\nu^4)^{1/4},$$
$$\Xi_\nu = \exp[-q_\nu\epsilon_\nu^2/q_{L\nu}w_\nu^2 + \xi_\nu^2(q_\nu/q_{L\nu})q_\nu/(q_\nu + q_{L\nu})]$$
$$= \exp[-(q_\nu/q_{L\nu})[\epsilon_\nu^2/w_\nu^2 - (1 + o_\nu^2)\xi_\nu^2/2]], \qquad (15)$$
$$M_{\mu\nu} = (2^\mu\mu!)^{-1/2}o_\nu{}^\mu H_\mu[\xi_\nu(1 + o_\nu^2)/\sqrt{2}o_\nu].$$

This rather cumbersome equation gives the response of the resonator to a misadjusted Gaussian input beam. It is not easily exploited. The factor $M_{\mu\nu}$, which governs the convergence of the series, does not generally converge monotonically (see Sec. VIII). It is, however, normalized in the sense that $M_{0\nu} = 1$. Also the requirement that $A_0 = 1$, $A_\mu = 0$ for perfect adjustment is satisfied.
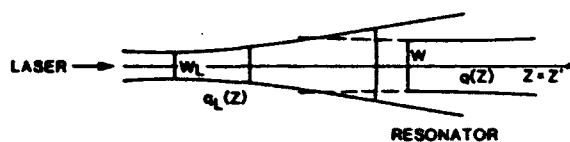
Fig. 3. Mismatched system: Laser and resonator have different waist sizes located at different z values. The system is aligned, however, i.e., $z = z'$.
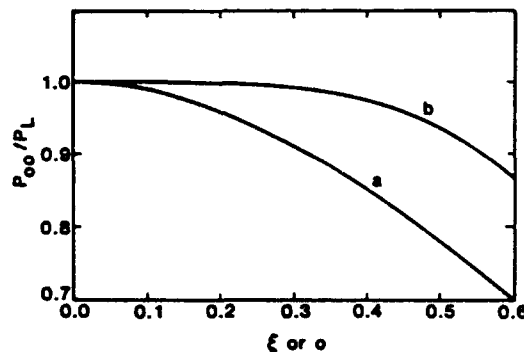
Fig. 4. Power transfer from the Gaussian laser beam to the Gaussian of the resonator in a misadjusted system: a, power transfer ratio in a misaligned system, where $\xi = (|\xi_x|^2 + |\xi_y|^2)^{1/2}$ is set. For $\xi \to 0$, $P_{00}/P_L \to 1$, asymptotically; b, power transfer in a mismatched system, where $o = o_x = o_y$ is set. Again there is asymptotic convergence for $o \to 0$.

VI. Power Transfer into the Resonator's Gaussian

This problem is of obvious interest for the design of such a system.

For the resonator Gaussian, $A_{00} = W_x W_y \Xi_x \Xi_y$. For perfect adjustment, $\xi_\nu = 0$, $q_\nu = q_{L\nu}$ (for both $\nu = x$ and $\nu = y$), $o_\nu = 0$, $A_{00} = 1$, and the power transfer is $P_{00}/P_L = |A_{00}|^2 = 1$.

In the special case of proper alignment (but mismatch), Eq. (15) produces with $\Xi_\nu = 1$ the simple result

$$P_{00}/P_L = |W_x|^2|W_y|^2 = ((|1 - o_x^4||1 - o_y^4|)^{1/2}(\epsilon_\nu = \alpha_\nu = 0, o \neq 0). \qquad (16)$$

The upper curve in Fig. 4 shows the power transfer vs o, where $o_x = o_y = o$. As Eq. (16) suggests the transfer is not very sensitive to small mismatch. For example, if the spot sizes of resonator and laser are 10% different, we obtain $P_{00}/P_L = 0.991$, i.e., <1% of the power is put into HGs. In the special case of proper match (but misalignment), we have, with $q_\nu = q_{L\nu}$, $W_\nu = 1$:

$$P_{00}/P_L = |\Xi_x|^2|\Xi_y|^2 = \exp[-(\epsilon_x^2/w_x^2 + k^2w_x^2\alpha_x^2/2^2)]$$
$$\times \exp[-(\epsilon_y^2/w_y^2 + k^2w_y^2\alpha_y^2/2^2)],$$
$$= \exp[-(|\xi_x|^2 + |\xi_y|^2)] \qquad (o = 0, \xi_\nu \neq 0) \qquad (17)$$

displayed as the lower curve in Fig. 4, where $\xi^2 = |\xi_x^2| +$

$|\xi_y^2|$ is set. Equation (17) shows again that offset and tilt are in quadrature. In a system with 10% misalignment ($\xi^2 = 0.1^2 = 0.01$), ~1% of the power is lost.

VII. Size of the Hermite-Gaussians in a Misadjusted System

To find the amplitudes of HGs ($m \neq 0$, $n \neq 0$), it is convenient to avoid factors which do not depend on m or n. We form

$$A_\mu/A_0 = M_{\mu\nu} = (o_\nu^\mu/2^{\mu/2}\sqrt{\mu!})H_\mu[\xi_\nu(1 + o_\nu^2)/\sqrt{2}o_\nu], \quad (18)$$

with the two special cases

$$A_\mu/A_0 = \xi_\nu^\mu/\sqrt{\mu!} \sim (2\pi\mu)^{-1/4}(e\xi_\nu^2/\mu)^{\mu/2}(match, o_\nu \to 0), \quad (19)$$

$$A_{2\rho}/A_0 = [(-1/2)^\rho\sqrt{(2\mu)!}/\mu!]o_\nu^{2\rho} \sim (-o_\nu^2)^\rho/(\pi\mu)^{1/4}, \quad (20)$$

$$A_{2\rho+1}/A_0 = 0 \text{ (alignment, } \xi_\nu \to 0).$$

Equations (19) are obtained using $H_\mu(\nu \to \infty) \sim (2\nu)^\mu$ and Stirling's approximation for the factorial Eqs. (20) by using $H_\mu(\nu \to o) \simeq (-1)^{\mu/2}\mu!/(\mu/2)!$ for even μ and $H_\mu(\nu \to o) \simeq 0$ for odd μ.

The asymptotic forms are given to demonstrate the fast convergence of the mode amplitudes, once near adjustment with $|\xi_\nu| \ll 1$, and $|o_\nu| \ll 1$ is achieved. They are, by the way, within 4% of the explicit forms for $\mu \geq 2$. Equations (20) also show that pure mismatch produces even-indexed HGs only, as opposed to pure misalignment. That odd-indexed HGs vanish in an aligned system follows directly from a consideration of the symmetry of an aligned beam with respect to both the x and y direction. Figure 5 show the isophotes of an offset beam which is also mismatched in the y direction but matched in the x direction. If the offset is removed, the lower part of the figure has the odd-indexed modes absent. Figure 6 gives a plot of the field vs x of an injected beam with the sizable offset $\xi_x = 1$, i.e., $\epsilon_x = w_x$. Note that the amplitude A_5 has already drastically decayed ($A_5/A_0 \simeq 0.09$); the power in the 5–0 mode is <1% of the power of the Gaussian mode.

As far as the phases are concerned, we note that, o_ν being either real or purely imaginary for a nearly matched system, the HGs for the aligned system [Eq. (20)] have either the same phase ($w_L > w$) or alternating signatures ($w_L < w$); for a misaligned system [Eq. (19)], the phases depend on the relative contribution of tilt and offset.

VIII. Application to Misadjusted Resonator System

In a ring interferometer the beam path encloses a finite area, and the modes are astigmatic. The injecting laser, therefore, needs to be matched in the x and y planes besides having to be aligned in both coordinates.

The identification of the modes in such an astigmatic cavity is done by evaluating the eigenfrequencies of the resonator. From Ref. 5 it follows that

$$f_{mnq} = (c/L)[(m + 1/2)\beta_x/2\pi + (n + 1/2)\beta_y/2\pi] + (c/L)q, \quad (21)$$

where the angles β_x and β_y depend on geometry and

OFFSET + Y-MISMATCH
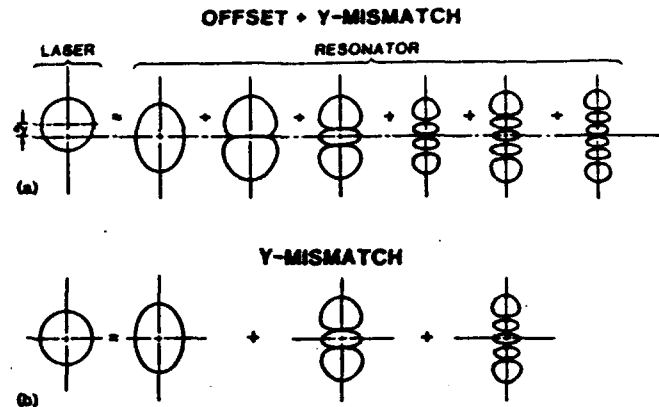
Y-MISMATCH

Fig. 5. Isophotes of laser beam and resonator modes with proper adjustment in the x direction. (a) Offset ϵ_y and mismatch o_y produce all $E_{0,n,q}$ modes in the resonator. (b) Mismatch alone produces only even-indexed Hermite-Gaussian modes. Since the system is perfectly adjusted in the x direction, all excited Hermite-Gaussians have $m = 0$.
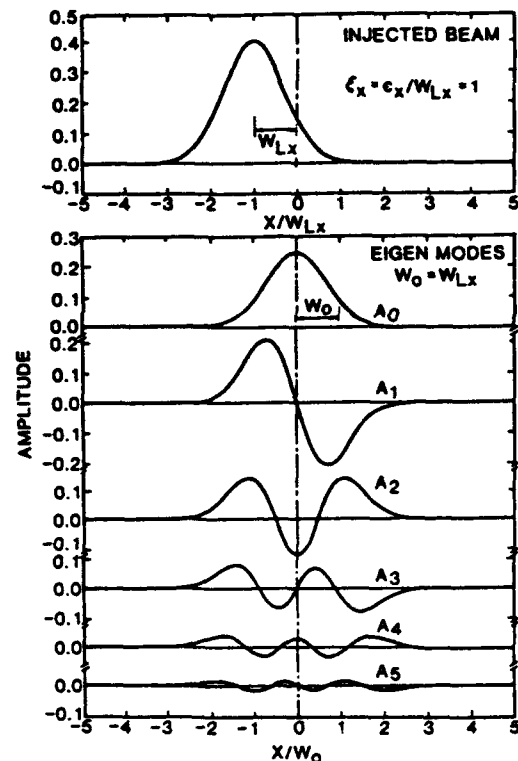
Fig. 6. Field distribution vs normalized x axis due to an offset beam with misalignment parameter $\xi_x = 1 + j0$ (pure offset, $\epsilon_x = w_{Lx}$). Shown is the incoming beam and the first five excited eigenmodes. All vertical scales are equal.

mirror curvature radii R. We analyzed a square ring[6] of perimeter $L = 3.15$ m, with two diagonally placed spherical mirrors of equal curvature radius $R = 6.00$ m. The other two mirrors are flat. The beam is injected at one of the flat mirrors. The frequency differences are

$$f_{mnq} - f_{00q} = (c/\pi L)[m \cos^{-1}(1 - L/\sqrt{2}R) + n \cos^{-1}(1 - L/2\sqrt{2}R)] \quad (22)$$
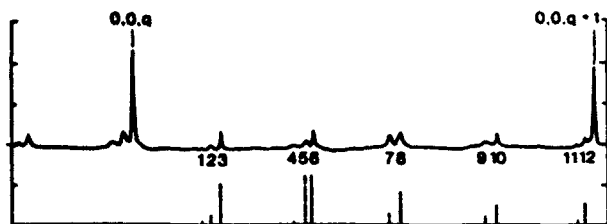
Fig. 7. Fabry-Perot scan of a misadjusted system. The two Gaussian modes $0,0,q$ and $0,0,q+1$ are prominent because the injected Gaussian beam is not far from adjustment. The identification of the peaks in the free spectral range of the resonator is

1	$0,11,q\text{-}2$	7	$0,8,q\text{-}1$	overlapping are	1	$2,3,q\text{-}1$	(?)
2	$0,6,q\text{-}1$	8	$0,3,q$	the following	4	$2,4,q\text{-}1$	
3	$0,1,q$	9	$0,9,q\text{-}1$	modes:	7	$2,0,q$	
4	$0,12,q\text{-}2$	10	$0,4,q$		9	$2,1,q$	(?)
5	$0,7,q\text{-}1$	11	$0,10,q\text{-}1$		11	$2,2,q.$	
6	$0,2,q$	12	$0,5,q;$				

The system has the two mismatch parameters $o_x = 0.53\text{-}j0.66$, $o_y = 0.40\text{-}j0.76$, and the two misalignment parameters $\xi_x = = 0+j0$ and $\xi_y = 0.255\text{-}j0.153$; the latter corresponds to an offset of 180 μm and a tilt angle of 49 sec of arc. The lower sequence are least-squares fitted amplitudes. The fit of the 0-n sequence has residuals of 2.4% average.

as shown in Fig. 7. In the free spectral range between the Gaussian $0,0,q$ and $0,0,q+1$ modes (q is unknown), seventeen modes are identified including $0,n,q$, modes ($n = 0\text{-}12$) and $2,n,q$ modes ($n = 0\text{-}4$).

The analysis proceeds as follows: The absence of the $1,n,q$ modes suggests alignment in the plane of the ring [Eq. (20)], $\epsilon_x = \alpha_x = 0$. The relatively large ratio of the $0,0,q$ modes to others suggests a near-adjusted situation, i.e., ϵ_y and α_y are small. The mismatch is known from the optical circuit: $o_x = 0.53\text{-}j0.66$ $o_y = 0.40\text{-}j0.76$. Thus we expect even-indexed modes to appear in both planes, i.e., $m = 2,4,6,\ldots$, as well as $n = 2,4,6\ldots$

The general Eq. (18) has to be applied for the y direction, whereas Eq. (20) is applicable to the HGs in the x direction. The unknown parameter is ξ_y.

In a least-squares fit, the nine largest measured ratios of the 0-n peaks to the 0-0 peak were fitted with the squared absolute value $|A_\mu/A_0|^2$ from Eq. (18) using the adjustable parameter ξ_y. The fit produced rms residuals of 2.4% (with respect to the 0-0 peak) with $|\xi_y| = 0.30$, and $\epsilon_y = 180\,\mu$m, $\alpha_y = 49$ arc-sec. These are plausible values, considering that even nuances of the spectrum were verified as, for example, the rank of almost every 0-n peak, although the series was not monotonic.

Of the five 2-n peaks, only the 2-0 peak is prominent. Nevertheless, Eq. (20) predicts these five peaks to within a factor of 2 assuming that the nearly coinciding 0-n lines have negligible powers. Figure 8 depicts the same system but with an improvement in the matching circuitry: A spherical lens had been put in a compromise position to effect a better match with the result $o_x = 0+j0.328$, $o_y = 0.303+j0$, ($|o_y| \simeq |o_x|$).

These values for mismatch are already quite low, although an effort has not yet been made in this experiment to inject an astigmatic beam. The calculated power transfer into the 0-0 mode is [Eq. (16)] $P_{oo}/P_L = 0.990$; i.e., only 1% of the power is lost.

Concurrently, a much better alignment has been achieved. The emergence of the 1-0 mode as well as the 0-1 mode signifies, however, that there is now misalignment in both planes. The estimates from these two small peaks are $|\xi_x| \sim 0.16$ and $|\xi_y| \simeq 0.19$. The paucity of the data does not allow determination of a real and imaginary part of ξ, i.e., of ϵ and α in Fig. 8. Further experiments to relate the Hermite-Gaussian mode structure to misadjustment are quite welcome.

IX. Discussion and Conclusion

The calculations presented in this paper allow a quantitative estimate of power matching as well as the prediction of the HG structure in a resonator excited by a misadjustment beam. The two complex parameters ξ (misalignment) and o (mismatch) have been introduced to account for offset, tilt, and mismatch. In an astigmatic system, a separate set of parameters is necessary for each of the two orthogonal planes.

The analysis of data obtained on the example, a square ring with a perimeter of 3.15 m available in the literature, demonstrates that quite detailed information can be obtained about the degree of adjustment of a system through this theory.

Such knowledge may be put to good use in the engineering of a precision instrument as, e.g., a large ring interferometer. The necessary precision of adjustment can be calculated through a consideration of the effects of misadjustment on the desired data.

The loss of power in the desired 0-0 mode is an obvious effect. It is itself Gaussian in the two parameters offset and tilt, whereby these parameters, which are in quadrature, are naturally measured with respect to spot size and beam divergence. For a mismatched beam the loss is proportional to o^4, meaning that power
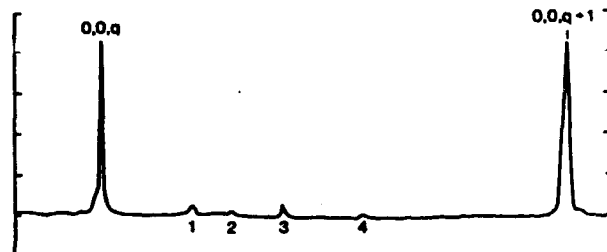
Fig. 8. Fabry-Perot scan of a better adjusted system (compare with Fig. 7). Both mismatch and misalignment are improved, the former by inserting a (spherical) lens in a compromise position. Identification of peaks: 1, $0,1,q$; 2, $1,0,q$; 3, $0,2,q$; 4, $2,0,q$. There is now misalignment and mismatch in both directions, although reduced. The parameters are (compare with Fig. 7) $o_x = 0+j0.33$, $o_y = 0.30+j0$; $|\xi_x| \simeq 0.16$, $|\xi_y| \simeq 0.19$. The near symmetry of o_x and o_y signifies that $q_L/q_y \sim q_x/q_L$; i.e., the mismatch has been properly distributed to the two directions.

loss becomes relatively harmless once $|\beta| \ll 1$ and $|\alpha| \ll 1$, near adjustment, is achieved.

Another effect to be considered is frequency pulling. If we define it as the difference δf between the frequency f_0 of a Gaussian with amplitude A_0 and the frequency of the composite peak due to the presence of a HG with frequency f_1 and amplitude A_1, we get for this kind of pulling $\delta f/f_0 = (A_1/A_0)(1/2Q)^4/(f_1/f_0 - 1)^3$, where $Q = f_0/\Delta f$ is the quality factor of the resonator. On the basis that δf ought to be less than a given value, A_1/A_0 can be estimated and the degree of necessary adjustment predicted.

The ambiguity of the ring's output due to the presence of several modes is to be considered as a sort of noise and again can be suppressed with proper adjustment techniques.

Finally we propose a control scheme for adjustment of the system injection resonator. It makes use of the orthogonality and symmetry of the modes with respect to specific misadjustments:

(1) Pick up the 0–1 mode from a scanner and control with it vertical alignment. Since offset and tilt are in quadrature, each type of misalignment can be adjusted separately.

(2) Use the 1–0 mode to control the horizontal alignment in a similar way.

Note that in particular any mismatch does not affect the amplitude of these two modes.

(3) Once these modes disappear, any residual 0–2 and 2–0 modes are then due to mismatch. Although we do not believe that a once-matched system goes into significant mismatch due to ambient effects, there is nevertheless the possibility of using these latter modes to control the match by using zoom systems with cylindrical lenses in the respective planes.

This work has been done under Air Force grant AFOSR 84-0058.

References

1. Several aspects of coupling and power conversion between modes have already been discussed by H. Kogelnik, "Coupling and Conversion Coefficients for Optical Modes," in *Proceedings, Symposium on Quasi-Optics, June 1964*, J. Fox, Ed. (Polytechnic Press, Brooklyn, N.Y., 1964), p. 333.
2. H. A. Haus, *Waves and Fields in Optoelectronics* (Prentice-Hall, Englewood Cliffs, N.J., 1984), Chap. 4.
3. A. E. Siegman, "Orthogonality Properties of Optical Resonator Eigenmodes," Opt. Commun. 31, 369 (1979).
4. I. S. Gradshteyn and I. M. Ryzhik, *Table of Integrals, Series, and Products* (Academic, New York, 1980). With the substitution $x = \sqrt{2}v/w_n$, integral Eq. (10) is transformed in an integral of the type 7.374, No. 10, p. 838.
5. S. A. Collins, "Analysis of Optical Resonators Involving Focusing Elements," Appl. Opt. 3, 1263 (1964).
6. T. D. Baxter, T. T. Saito, G. L. Shaw, R. T. Evans, and R. A. Motes, "Mode Matching for a Passive Resonant Ring Laser Gyroscope," Appl. Opt. 22, 2487 (1983).

annealing, and condensed matter studies. This final chapter is in my opinion too limited; the explanation may simply be a question of space and emphasis. It undoubtedly opens the arena for a more comprehensive review of excimer laser applications in basic science and technology. It is precisely the widespread use of excimer lasers in medicine, materials processing laser-assisted chemical vapor deposition, lithography, etching, and weapons research that has made the transition of excimer laser devices from laboratory curiosity to useful tool. This chapter should foster further basic research and the development of the next generation of excimer lasers. Another research area noticeably absent from this chapter is the prolific use of excimer lasers in reaction dynamics and photodissociation studies.

As a whole the book will provide an extremely useful source (albeit in some areas not too updated) of information and reference for the beginner and the specialist whose research or occupation involves utilization or development of excimer lasers.

ERNESTO E. MARINERO

Hot-Electron Transport in Semiconductors. Edited by L. REGGIANI. Springer-Verlag, Heidelberg, 1985. 275 pages. $42.00.

The field of hot-electron transport in semiconductors has become one of the most important elements in modern electronic device theory. This has always been an interesting field of study from an academic point of view, and high field transport enjoyed a flurry of activity in the 1960s due to the discovery of the Gunn effect. However, practical applications to the broad range of electronic devices were minor until recently. With the advent of fine-line geometries in silicon and gallium arsenide transistors and integrated circuits, however, modern devices increasingly operate in the hot-electron regime. Simultaneously, the development of multilayer heterostructures in III–V compounds grown by molecular beam epitaxy (MBE) and organometallic chemical vapor deposition (OMCVD) has introduced extremely small geometries in the vertical dimension. As a result, most of the new device structures currently under investigation depend on hot-electron transport for their operation.

After many years of work on what was considered interesting but not very practical subjects, hot-electron transport theorists are suddenly in great demand, and their understanding of high-field transport is crucial to modern device conception and development.

This book—Vol. 58 in Topics in Applied Physics—is a brief but extremely useful summary of some of the major topics of carrier transport at high fields. The contributors are well known in the field, and they have done an excellent job of presenting their areas of specialization succinctly and with the nonspecialist in mind. The general problem of hot-electron transport is described by Reggiani, including a summary of scattering mechanisms and an introduction to the Monte Carlo method for calculating carrier transport. Chapters follow on the measurement of transport parameters by time-of-flight, microwave, and noise measurements. Later chapters deal with the distributions of hot electrons in multivalley semiconductor bands at high fields and the streaming motion of carriers in crossed electric and magnetic fields. The applications of hot-electron theories to modern semiconductor devices are discussed in the final two chapters in terms of heterostructure superlattices and submicron device structures.

This book is appropriate reading for anyone involved in semiconductor device research who is called on to understand carrier transport in small-geometry structures. It is hard to imagine invention of